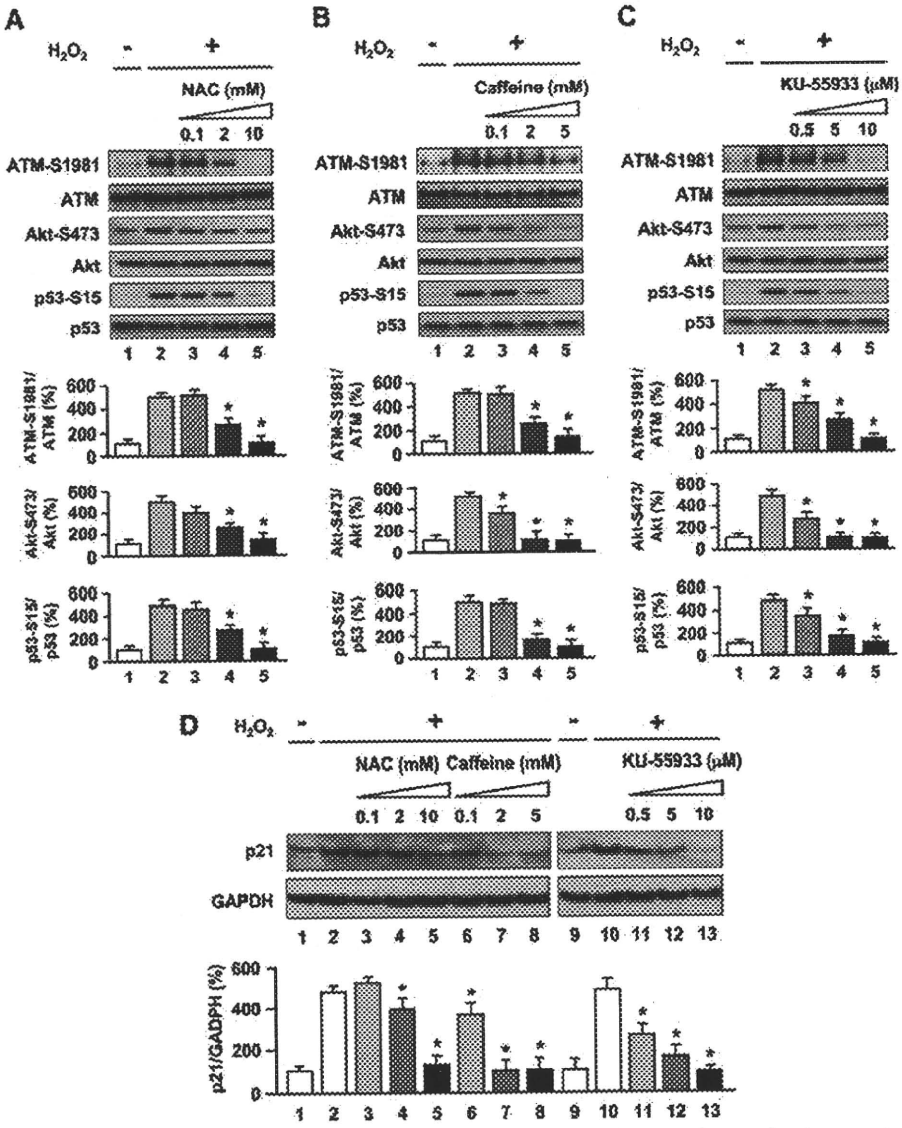

FIGURE 2. **Oxidative stress-induced Akt and p53 phosphorylation and up-regulation of p21 expression are dependent on ATM kinase.** *A–C*, antioxidant and ATM inhibitors blocked phosphorylation of ATM-S1981, Akt-S473, and p53-S15 as stimulated by H_2O_2 exposure. Cells were treated with 100 μM H_2O_2 for 30 min in the absence or presence of NAC (*A*) or caffeine (*B*), or KU-55933 (*C*), and whole cell lysates were subjected to Western blot analyses using the indicated antibodies. *D*, antioxidant and ATM inhibitors down-regulated p21 induction as stimulated by H_2O_2 exposure. Cells were pretreated with NAC, caffeine, or KU-55933 and then 100 μM H_2O_2 for 3 h. Whole cell lysates were subjected to Western blot analyses using p21 antibody. GAPDH was used as loading control. Values are mean ± S.E. (*error bars*) ($n = 3$). *, $p < 0.05$ *versus* cells incubated with H_2O_2. Representative blots are shown in the *upper panels* whereas corresponding quantitation is shown in the *lower panels*.

labeled polymer. Finally, sections were incubated with diaminobenzidine tetrahydrochloride (Dako Japan), and the nuclei were counterstained with hematoxylin.

Statistical Analysis—All values are expressed as mean ± S.E. Differences between two groups were analyzed using the two-tailed Student's *t* test. Threshold of significance was taken as $p < 0.05$.

RESULTS

ATM Is Activated by Oxidative Stress in Vascular Endothelial Cells—To investigate the involvement of ATM in mediating oxidative stress in the vasculature, we first examined the activation and expression of ATM in cultured HUVECs treated with H_2O_2 as an inducing agent of oxidative stress. HUVECs exposed to H_2O_2 showed increased ATM phosphorylation at Ser^{1981} (ATM-S1981) (Fig. 1, *A* and *B*), which releases it from an inhibitory homodimer structure leading to its activation and recruitment to sites of DNA double-strand breaks (DSBs) (12–14). We next investigated factors involved in the ATM signaling pathway. Because ATM mediates activation of Akt in response to insulin or ionizing radiation which then in turn results in radiosensitivity or resistance to insulin in cell lines derived from A-T patients and ATM knock-out mice (15), we first investigated the activation of Akt in response to oxidative stress. Akt phosphorylation at Ser^{473} (Akt-S473) was increased in H_2O_2-treated HUVECs (Fig. 1, *A* and *B*). We then investigated involvement of p53, a downstream signaling molecule of ATM (10) and Akt (6), which showed phosphorylation at Ser^{15} (p53-S15) after exposure to H_2O_2 (Fig. 1, *A* and *B*). Furthermore, p21, a downstream target of p53, was increased in H_2O_2-treated HUVECs (Fig. 1*C*). Our results indicate that oxidative stress phosphorylates ATM and its involved genes, Akt and p53, with subsequent up-regulation of p21 expression. Thus, the phosphorylation of ATM, Akt, and p53 and up-regulation of p21 expression mediate actions of oxidative stress in endothelial cells.

Although ATM is predominantly present in the nucleus, a variable amount (<10%) has been reported in the cytoplasm, especially in neuronal cells. The major known role of nuclear ATM is to participate in the response to DSBs for DNA repair and cell cycle checkpoint activation (16). In response to agents that induce DSBs, ATM has been found to relocalize to the sites of breaks and in doing so forms large nuclear foci (17). To determine whether oxidative stress-induced ATM forms foci, immunofluorescence analyses for phospho-ATM (Ser^{1981}), total ATM, and p21 were performed. Increased fluorescence and foci formation were seen in response to H_2O_2 for phosphorylated ATM (Fig. 1*E* and supplemental Fig. 1*B*) and increased p21 (Fig. 1*G* and supplemental Fig. 1*D*) under conditions in which 53BP1 formed nuclear foci in response to etoposide as reported

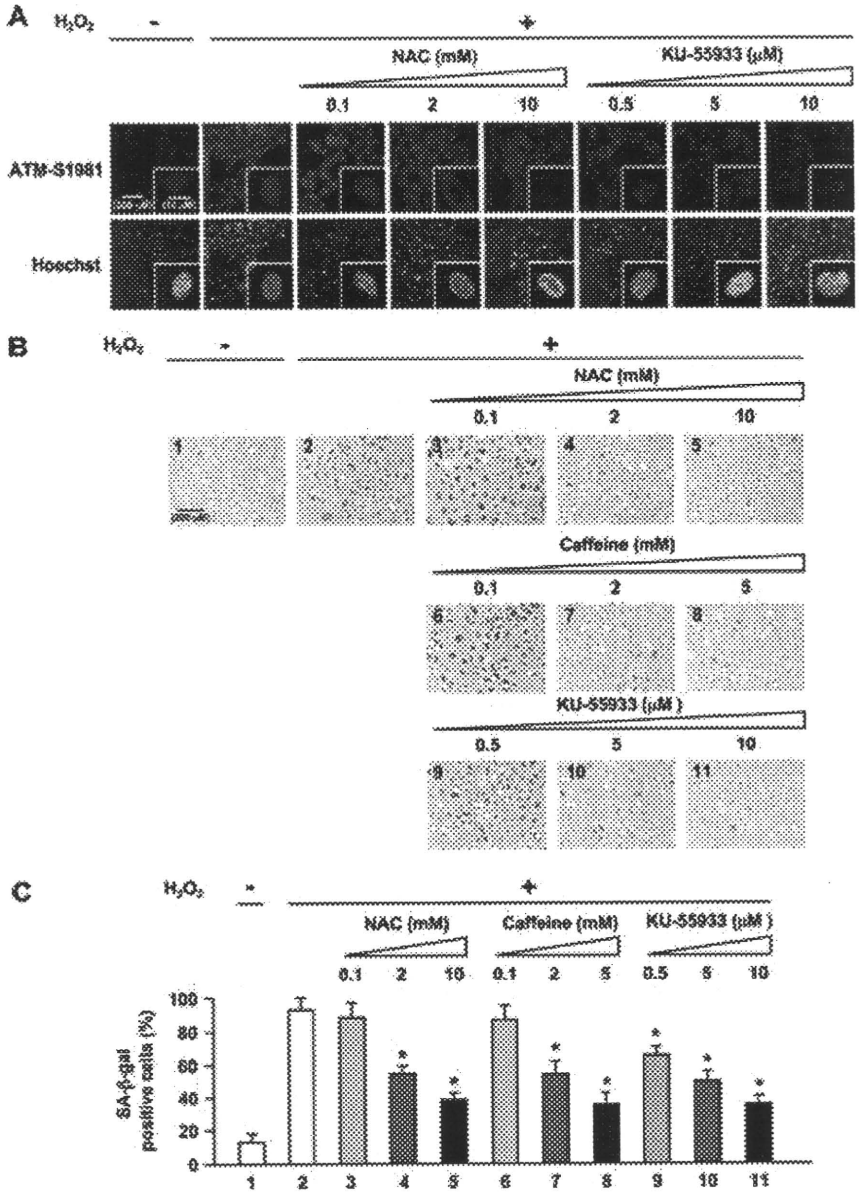

FIGURE 3. **Oxidative stress-induced endothelial cell senescence involves activation of ATM kinase.** *A*, immunofluorescence analysis of the effects of antioxidant (NAC) and ATM inhibitor (KU-55933) on phosphorylated ATM. Cells were treated with NAC or KU-55933 followed by 100 μM H_2O_2 for 1 h and then immunostained for phosphorylated ATM-S1981. Hoechst 33258 was used as nuclear stain (*blue*). Original magnification, ×200 and ×630. Higher magnification of the representative cells in *A* is shown in supplemental Fig. 2. *Scale bar*, 200 μm and 10 μm, respectively. NAC or KU-55933 greatly reduced phosphorylated ATM nuclear fluorescence and foci formation. *B*, effects of NAC, caffeine, or KU-55933 on premature senescent phenotype induced by H_2O_2 as shown by SA-β-gal staining. *C*, quantification of percentage of SA-β-gal-positive cells in *B*. Values are mean ± S.E. (*error bars*) ($n = 3$). *, $p < 0.05$ *versus* cells incubated with H_2O_2. Original magnification, ×100. *Scale bar*, 200 μm. Pretreatment with NAC, caffeine, or KU-55933 resulted in significant reduction of senescent (SA-β-gal-positive) cells compared with those exposed to H_2O_2 alone.

(Fig. 1*D* and supplemental Fig. 1*A*) (18). Total ATM, in contrast, remained diffusely localized throughout the nucleus, and foci formation was not observed in H_2O_2-treated HUVECs (Fig. 1*F* and supplemental Fig. 1*C*). Activated (phosphorylated) ATM localized to foci, which suggests that it might be recruited to sites of DNA damage caused by oxidative stress (17, 18). However, the authors note that the antibody used (ATM-S1981) is known to also recognize a nonspecific protein, which makes conclusions based on experiments using this antibody inconclusive. We further investigated expression of 53BP1 and γ-H2AX as markers of DSB formation in response to H_2O_2 by immunostaining. In the H_2O_2-treated cells, both 53BP1 and γ-H2AX formed nuclear foci (supplemental Fig. 3), which further supports that ATM is activated in response to DSB formation induced by H_2O_2.

Activation of the ATM-dependent DNA Damage Signaling Pathway Contributes to Endothelial Cell Senescence—To better confirm actions of activation of ATM by oxidative stress in endothelial cells, effects of inhibitors of oxidative stress and of ATM were tested. HUVECs were pretreated with NAC, an antioxidant and glutathione precursor that alters the redox state of cells (19), to assess whether ATM phosphorylation was caused by H_2O_2-induced redox imbalance. Western blot analysis showed that pretreatment of endothelial cells with NAC blocked the stimulatory effects of H_2O_2 on the expression of ATM-S1981, Akt-S473, p53-S15 (*lanes 3–5* in Fig. 2*A*) and p21 (*lanes 3–5* in Fig. 2*D*). These results suggest a direct role of H_2O_2 in ATM phosphorylation and activation of involved genes. We further employed two inhibitors, caffeine and KU-55933, to inhibit ATM kinase activity to examine whether Akt and p53 activation as well as p21 up-regulation induced by H_2O_2 is dependent on the ATM protein kinase. Caffeine is known to disrupt ATM-dependent responses likely through direct inhibition of ATM kinase activity (20), and KU-55933 is a specific and potent inhibitor of ATM kinase (21). Both inhibitors inhibited H_2O_2-induced ATM (Ser^{1981}), Akt (Ser^{473}), and p53 (Ser^{15}) phosphorylation (*lanes 3–5* in Fig. 2, *B* and *C*), in addition to p21 induction (*lanes 6–8* and *lanes 11–13* in Fig. 2*D*). Thus, ATM kinase played a major role in transducing H_2O_2-induced DNA damage signaling in HUVECs. Because an Akt/p53/p21-dependent pathway has been reported in endothelial cells (6), ATM thus likely regulates the cellular response to oxidative stress via phosphorylation of Akt and p53 then induction of p21 in sequence. Furthermore, NAC or KU-55933 also

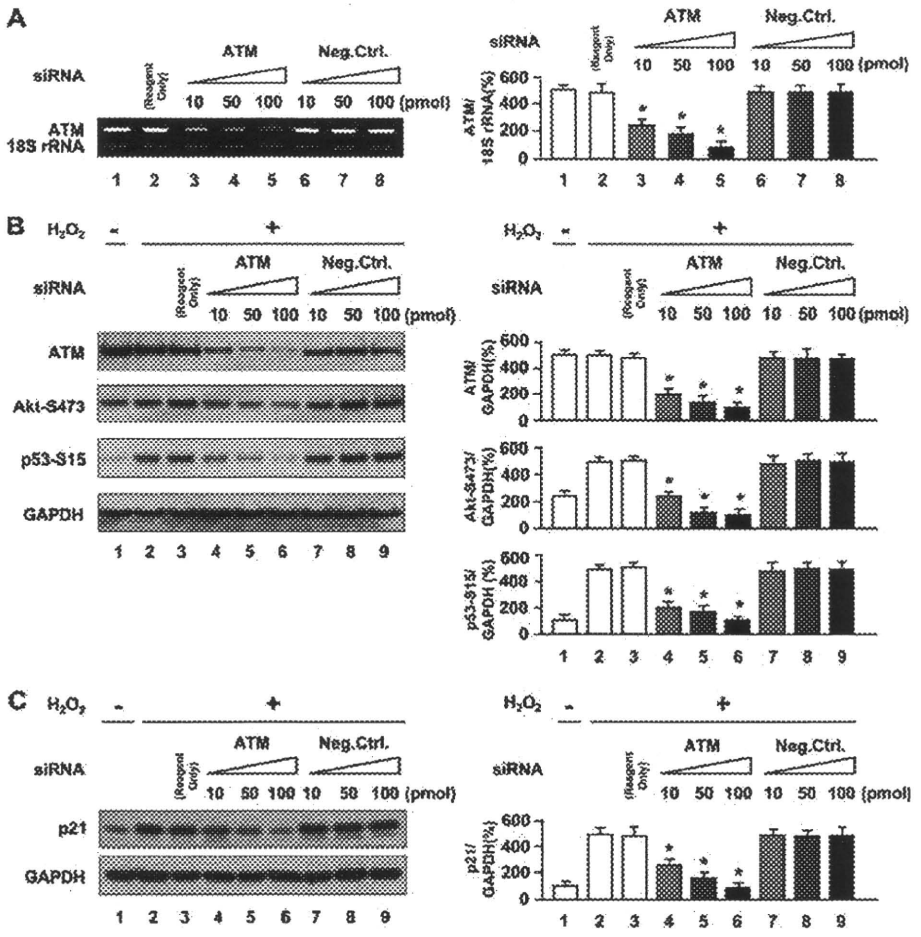

FIGURE 4. **Knockdown of ATM by ATM siRNA inhibits oxidative stress-induced activation of Akt and p53 and induction of p21 expression.** *A*, effect of siRNA against ATM on expression of ATM as analyzed by RT-PCR. *B* and *C*, Western blot analysis of the effects of siRNA against ATM on expression of total ATM, Akt phosphorylation (Ser^{473}), p53 phosphorylation (Ser^{15}), and p21 induction. Cells were transfected with siRNA against ATM for 72 h followed by incubation with 100 μM H_2O_2 for 30 min in *B* or 3 h in *C*. GAPDH was used as loading control. Values are mean ± S.E. (*error bars*) ($n = 3$). *, $p < 0.05$ *versus* cells transfected with the same concentration of negative control siRNA. Representative blots are shown in the *left panels* whereas corresponding quantitations are shown in the *right panels*. *Reagent Only*, cells transfected with Lipofectamine 2000 alone.

greatly reduced phosphorylated ATM nuclear fluorescence and foci formation (Fig. 3*A*). Collectively, H_2O_2 induced DNA damage and stimulated autophosphorylation of ATM in addition to formation of discrete nuclear foci together with subsequent induction of phosphorylation of Akt, p53, and up-regulation of p21 expression in an ATM-dependent manner.

Because the DNA damage response pathway triggers senescence (22) and because p53 and p21 were described to be major players in the induction of senescence (23, 24), we next addressed the functional effects of activation of the ATM/Akt/p53/p21 pathway on endothelial cells, namely in the form of induction of senescence which is a consequence of endothelial dysfunction. We induced premature endothelial senescence by addition of H_2O_2 to 100 μM as shown by SA-β-gal assay, a recognized surrogate index of senescent cells (25). We found that percentage of HUVECs positive for SA-β-gal was markedly increased in cells treated with H_2O_2, compared with cells incubated without H_2O_2 treatment (*panel* 2 in Fig. 3*B* and *lane* 2 in Fig. 3*C*). Furthermore, pretreatment with NAC, caffeine, or KU-55933 resulted in significant reduction of senescent (SA-β-gal-positive) cells compared with those exposed to H_2O_2 alone (Fig. 3, *B* and *C*). Thus, activation of ATM by H_2O_2 promotes endothelial cell senescence and contributes to vascular pathogenesis.

Abrogation of ATM Blocks Effects of Oxidative Stress on Endothelial Cells—We further examined the requirement of ATM expression in H_2O_2-induced premature senescence by abrogating ATM in cells using RNA interference. Knockdown of ATM in HUVECs by siRNA reduced ATM mRNA and protein levels (Fig. 4, *A* and *B*). Cells transfected with ATM siRNA showed reduced ATM expression with inhibition of Akt and p53 phosphorylation (*lanes* 4–6 in Fig. 4*B*) in addition to down-regulation of p21 expression (*lanes* 4–6 in Fig. 4*C*). As expected, ATM nuclear fluorescence was also markedly decreased in cells with ATM knocked down (Fig. 5*A*). Furthermore, knockdown of ATM by siRNA suppressed increase in SA-β-gal-positive cells induced by H_2O_2 (*panels* 5 and 6 in Fig. 5*B* and *lanes* 5 and 6 in Fig. 5*C*), which were comparable with the changes seen when HUVECs were treated with antioxidant or ATM inhibitor. Moreover, down-regulation of Akt, p53, or p21 by siRNA also suppressed an increase in SA-β-gal-positive cells induced by H_2O_2 (supplemental Figs. 4 and 5). Thus, RNA interference experiments further confirmed that ATM and its downstream molecules, Akt, p53, and p21, mediate actions of oxidative stress on endothelial cells to induce senescence.

Abrogation of Senescent Phenotype in Aorta of ATM Knock-out Mice—To test whether ATM mediates vascular endothelial cell senescence *in vivo*, we administered STZ to ATM knock-out mice and wild-type littermates to induce hyperglycemia-induced endothelial dysfunction because vascular endothelial cell senescence has been previously documented to be induced in STZ-diabetic mice (26). Western blot analysis for ATM protein levels in the thoracic aortas of heterozygous knock-out mice showed marked reductions to levels almost comparable with those of homozygote knock-out mice in contrast to robust levels as seen in wild-type mice (Fig. 6*B* and supplemental Fig. 7*A*) although the mechanisms of reduced protein levels in heterozygous knock-out mice are unclear. STZ-treated mice showed an elevation in blood glucose levels compared with STZ-untreated mice (*lanes* 2, 4, and 6 in Fig. 6*C*). SA-β-

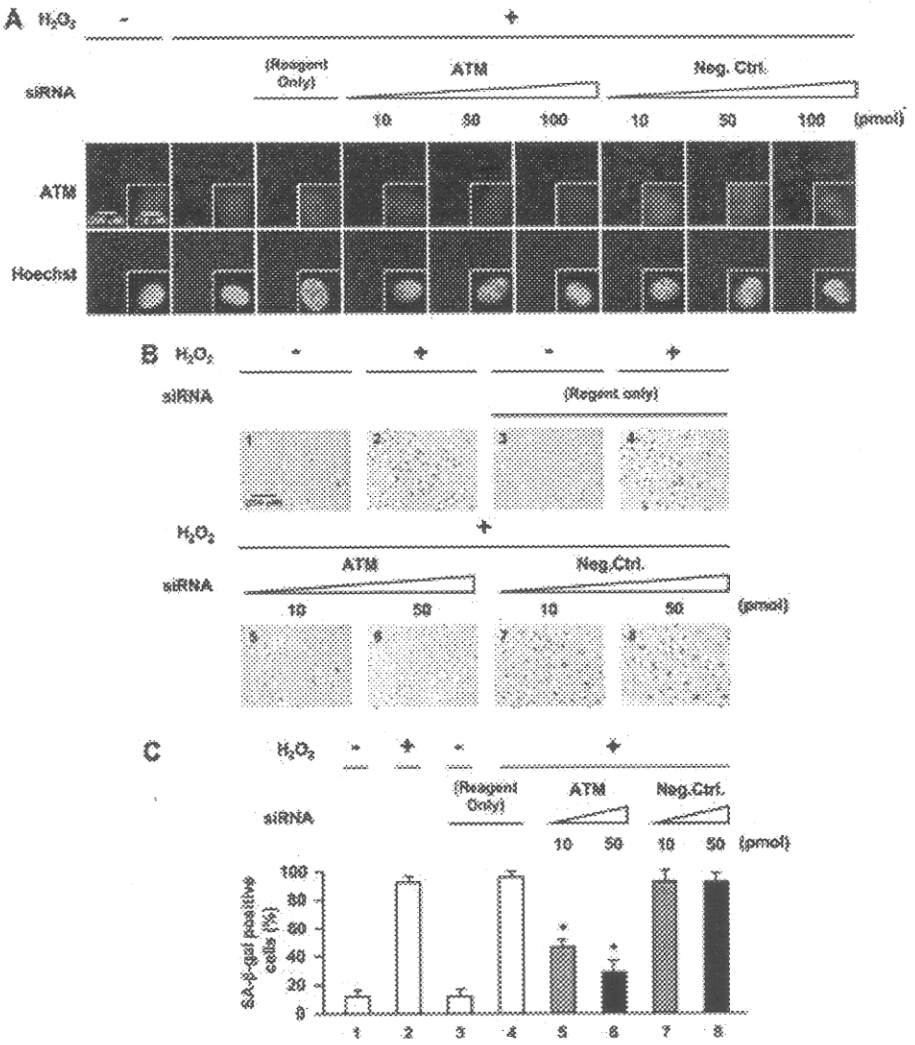

FIGURE 5. **Effects of abrogation of ATM expression by siRNA against ATM in oxidative stress-induced endothelial senescence.** *A*, immunofluorescence analysis of the effect of siRNA against ATM on total ATM. Transfected cells were immunostained for total ATM. Hoechst 33258 was used as nuclear stain (*blue*). Original magnification, ×200 and ×630. *Scale bar*, 200 μm and 10 μm, respectively. ATM nuclear fluorescence was greatly decreased in ATM knock-down cells. *B*, staining of SA-β-gal activity in ATM knock-down cells. *C*, quantification of percentage of SA-β-gal-positive cells in ATM knock-down cells. Values are mean ± S.E. (*error bars*) ($n = 3$). *, $p < 0.05$ *versus* cells transfected with the same concentration of negative control siRNA (*lane 7* or *lane 8*, respectively) ($n = 3$ each). Original magnification, ×100. *Scale bar*, 200 μm. *Reagent Only*, cells transfected with Lipofectamine 2000 alone. Knockdown of ATM by siRNA suppressed the increase in SA-β-gal-positive cells induced by H_2O_2.

gal activity was observed in the thoracic aortas of STZ-diabetic wild-type mice but not in STZ-diabetic ATM knock-out mice (Fig. 6, *D* and *E*). Cross-sections of thoracic aortas stained with SA-β-gal showed that positive areas were mostly localized to the luminal surface (Fig. 6*F*) which also stained positive for von Willebrand factor, indicating localization to vascular endothelial cells and not the extracellular matrix compared with normal rabbit IgG antibody (Fig. 6*G* and supplemental Fig. 6*A*). p21 and p16 are cyclin-dependent kinase inhibitor genes that are used as senescence markers. SA-β-gal-positive areas of cross-sections of thoracic aortas stained positive for p21 and p16 (Fig. 6*H* and 6*I*) but not for normal mouse IgG antibody used as a negative control (supplemental Fig. 6*B*). These results indicate that ATM is important for the induction of endothelial cell senescence in aortas of STZ-diabetic mice, which is consistent with *in vitro* cellular experiments.

DISCUSSION

Oxidative stress caused by reactive oxygen species plays an important causal role in senescence and age-related vascular diseases, including atherosclerosis and diabetic vasculopathy (7, 27, 28). Despite the wealth of knowledge on the effects and actions of oxidative stress on endothelial cells, characterization of involved regulatory pathways allowing for targeted molecular intervention with therapeutic intent had remained elusive.

We showed that ATM is involved in oxidative stress-induced endothelial dysfunction and premature senescencethroughanAkt/p53/p21-dependent pathway. Cellular experiments using HUVECs showed that the ATM/Akt/p53/p21 pathway was involved in oxidative stress-induced cellular senescence *in vitro*. Experiments using antioxidant and specific ATM inhibitory compounds or siRNA against ATM inhibited oxidative stress-induced cellular senescence thus confirming involvement of ATM and its dependent pathway. Furthermore, ATM induced endothelial cellular senescence *in vivo* in the aorta of diabetic wild-type mice but not in ATM knock-out mice. STZ-diabetic $ATM^{+/-}$ mice exhibit reduction in SA-β-gal-positive cells to levels almost comparable with those seen in STZ-diabetic $ATM^{-/-}$ mice. Reduction of ATM protein expression in heterozygote knock-out mice may account for the difference seen in endothelial senescence between wild-type and heterozygous knock-out mice. Collectively, the findings presented here indicate the importance of ATM in the induction of endothelial cell senescence induced by oxidative stress and abrogation of ATM resulting in a dysregulated response to pathophysiological stress in cardiovascular endothelial cells.

We further showed that ATM lies upstream from the Akt/p53/p21 pathway and that oxidative stress as sensed through ATM possibly in response to oxidative DNA damage is the initiating "trigger" and plays an instructive role in activation of this signaling pathway. Previous studies also demonstrated that ATM is a major upstream activator of Akt through control of

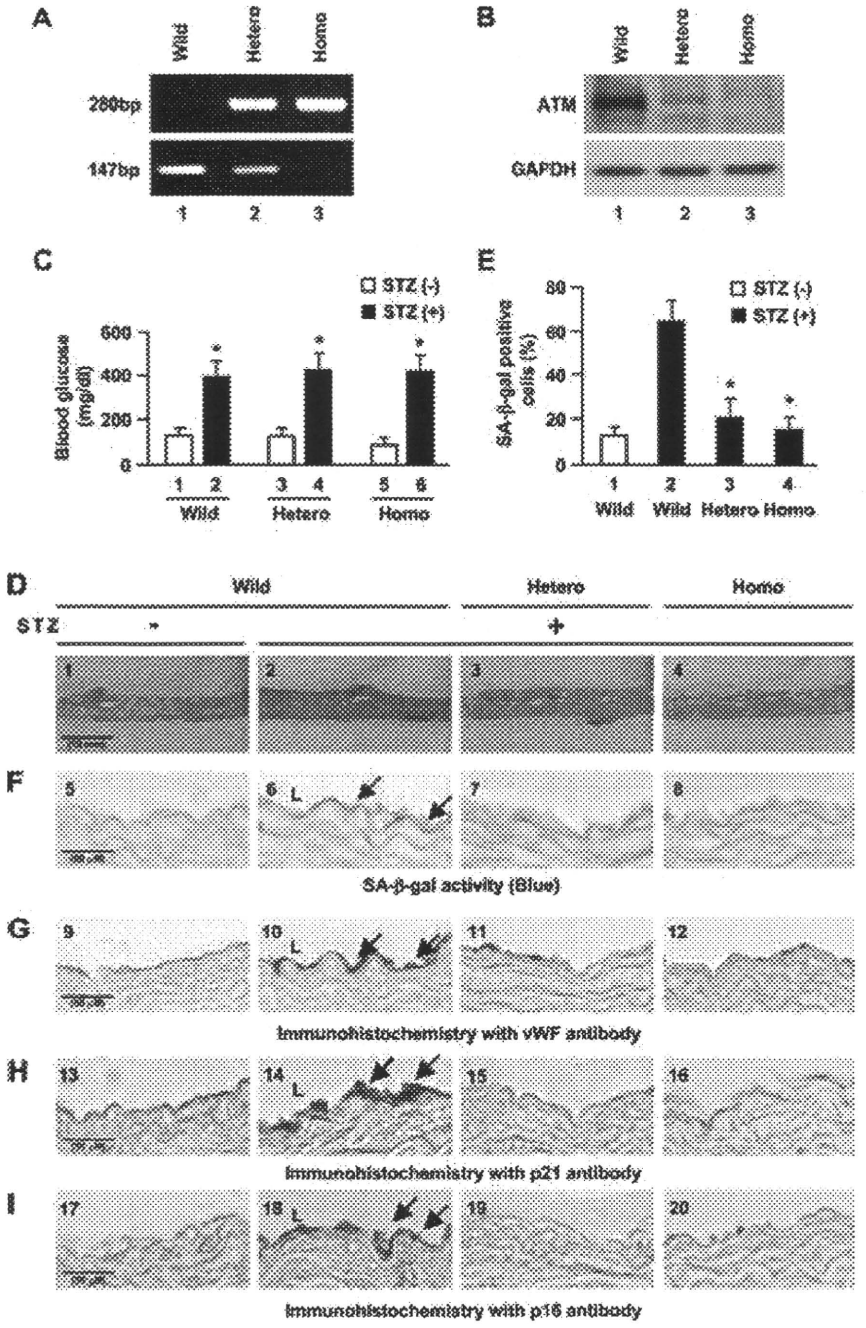

FIGURE 6. **Senescent endothelial cells in aortas of STZ-diabetic ATM knock-out mice.** Six respective $ATM^{+/+}$ (*Wild*), $ATM^{+/-}$ (*Hetero*), and $ATM^{-/-}$ (*Homo*) mice were used. *A*, genotyping analysis for ATM mice. *B*, Western blot analysis of ATM expression in the thoracic aortas. *C*, blood glucose levels measured before and after treatment with STZ. Values are mean ± S.E. (*error bars*). *, $p < 0.05$ *versus* STZ (−) mice (*lane 1*, *lane 3*, or *lane 5*, respectively). *D*, SA-β-gal activity (*blue*) in the thoracic aortas from mice at 10 days after treatment with STZ. *E*, quantitation of percentage of SA-β-gal-positive cells in the STZ-treated thoracic aortic samples. Values are mean ± S.E. *, $p < 0.05$ *versus* STZ (+) mice. *F*, sections of SA-β-gal stained thoracic aortas. *Arrows* indicate SA-β-gal-positive cells mostly localized to the luminal surface in the cross-section of the thoracic aortas. *G*, immunohistochemistry for von Willebrand factor, an endothelial cell marker, in the thoracic aortas (*brown*). *Arrows* indicate positive staining in the endothelium. *H* and *I*, immunohistochemical staining of p21 and p16 (*brown*). *Scale bar*, 50 μm and 10 mm, respectively.

Ser^{473} phosphorylation in response to insulin or ionizing radiation, which results in radiosensitivity or resistance to insulin in cell lines derived from A-T patients and ATM knock-out mice (15) or in muscle cells (29). However, in vascular endothelial cells stimulated by oxidative stress, we demonstrated for the first time to our knowledge that ATM regulates endothelial senescence through activation of Akt. Further, the pathway downstream of Akt through p53 and p21 has been well studied as a central pathophysiological signaling pathway in endothelial cells, especially in response to insulin (6, 7). However, whether the Akt/p53/p21 pathway is also activated by oxidative stress has not been clear. Our results thus indicate that this pathway is activated by oxidative damage and most importantly, regulated by ATM. γ-H2AX and 53BP1 foci formation was induced by oxidative stress, thus further providing supportive evidence that the oxidative stress-induced ATM-Akt/p53/p21 pathway is activated by DNA DSBs (supplemental Fig. 3).

Although the DNA damage response has been pursued mainly in oncogenesis and cancer-related fields and recently in regulation of senescence (1–3), as ATM has been shown to be activated by oxidative stress in hematopoietic cells (8), it is not beyond reason and in fact quite reasonable that ATM and the DNA damage response are involved in the vasculature as a response to oxidative stress albeit unexpected and unappreciated. Previous studies by ourselves initially suggested that the DNA damage response is activated in cardiovascular pathogenesis through the action of poly(ADP-ribose)polymerase-1 (PARP-1) (30), but identification and characterization of the actions of the central signaling molecule, ATM, in cardiovascular regulation provides further compelling evidence for the importance of this pathway in regulation of the vasculature and its diseases.

Our findings might explain in part the underlying mechanisms of the congenital disease condition of A-T in which the ATM gene is mutated. One of the hallmark characteristic phenotypes of A-T is vascular dysplasia and dysfunction, which pronounces as telangiectasia. Pathologically, vascular degeneration as characterized by loss of elastic fibers and proliferation of smooth muscle cells is seen. Patients that sur-

vive to later years are also known to be prone to ischemic heart disease (31). Although the precise underlying mechanism for the latter is unknown, in general, progression of coronary artery disease involves accelerated atherosclerosis in which oxidative stress of the endothelium and related cells plays a major contributory role. Response to oxidative stress in the vasculature may be disrupted in A-T patients. Dysregulation of endothelial cell function might lead to pathophysiological states such as vascular dysfunction in developmental states and accelerated atherosclerosis in adults. Better understanding the cellular response to oxidative stress with a focus on ATM is expected to shed further light on the pathogenesis of A-T and to clarify alternative pathological pathways that are activated in response to oxidative stress when deficient for ATM as well as to provide new insight into the molecular mechanisms underlying age-related cardiovascular pathologies such as atherosclerosis in which ATM might pose a new therapeutic target for vascular pathologies involving oxidative stress.

In conclusion, we show that oxidative stress can induce cellular senescence in HUVECs as shown by staining for SA-β-gal, which was associated with an ATM-dependent Akt/p53/p21 signaling pathway. Our findings might in part explain underlying mechanisms of the pathogenesis of the disease ataxia telangiectasia in which vascular dysplasia and dysfunction are seen, as well as suggesting that ATM may be a new therapeutic target for cardiovascular pathologies.

REFERENCES

1. Bartkova, J., Rezaei, N., Liontos, M., Karakaidos, P., Kletsas, D., Issaeva, N., Vassiliou, L. V., Kolettas, E., Niforou, K., Zoumpourlis, V. C., Takaoka, M., Nakagawa, H., Tort, F., Fugger, K., Johansson, F., Sehested, M., Andersen, C. L., Dyrskjot, L., Ørntoft, T., Lukas, J., Kittas, C., Helleday, T., Halazonetis, T. D., Bartek, J., and Gorgoulis, V. G. (2006) *Nature* **444,** 633–637
2. Bartkova, J., Horejsí, Z., Koed, K., Krämer, A., Tort, F., Zieger, K., Guldberg, P., Sehested, M., Nesland, J. M., Lukas, C., Ørntoft, T., Lukas, J., and Bartek, J. (2005) *Nature* **434,** 864–870
3. Gorgoulis, V. G., Vassiliou, L. V., Karakaidos, P., Zacharatos, P., Kotsinas, A., Liloglou, T., Venere, M., Ditullio, R. A., Jr., Kastrinakis, N. G., Levy, B., Kletsas, D., Yoneta, A., Herlyn, M., Kittas, C., and Halazonetis, T. D. (2005) *Nature* **434,** 907–913
4. Zeiher, A. M., Drexler, H., Saurbier, B., and Just, H. (1993) *J. Clin. Invest.* **92,** 652–662
5. Breitschopf, K., Zeiher, A. M., and Dimmeler, S. (2001) *FEBS Lett.* **493,** 21–25
6. Miyauchi, H., Minamino, T., Tateno, K., Kunieda, T., Toko, H., and Komuro, I. (2004) *EMBO J.* **23,** 212–220
7. Minamino, T., and Komuro, I. (2007) *Circ. Res.* **100,** 15–26
8. Ito, K., Hirao, A., Arai, F., Matsuoka, S., Takubo, K., Hamaguchi, I., Nomiyama, K., Hosokawa, K., Sakurada, K., Nakagata, N., Ikeda, Y., Mak, T. W., and Suda, T. (2004) *Nature* **431,** 997–1002
9. Barzilai, A., Rotman, G., and Shiloh, Y. (2002) *DNA Repair* **1,** 3–25
10. Shiloh, Y. (2003) *Nat. Rev. Cancer* **3,** 155–168
11. Ota, H., Eto, M., Kano, M. R., Ogawa, S., Iijima, K., Akishita, M., and Ouchi, Y. (2008) *Arterioscler. Thromb. Vasc. Biol.* **28,** 1634–1639
12. Bakkenist, C. J., and Kastan, M. B. (2003) *Nature* **421,** 499–506
13. Kozlov, S. V., Graham, M. E., Peng, C., Chen, P., Robinson, P. J., and Lavin, M. F. (2006) *EMBO J.* **25,** 3504–3514
14. Dupré, A., Boyer-Chatenet, L., and Gautier, J. (2006) *Nat. Struct. Mol. Biol.* **13,** 451–457
15. Viniegra, J. G., Martínez, N., Modirassari, P., Losa, J. H., Parada Cobo, C., Lobo, V. J., Luquero, C. I., Alvarez-Vallina, L., Ramón y Cajal, S., Rojas, J. M., and Sánchez-Prieto, R. (2005) *J. Biol. Chem.* **280,** 4029–4036
16. Lavin, M. F. (2008) *Nat. Rev. Mol. Cell Biol.* **9,** 759–769
17. Bencokova, Z., Kaufmann, M. R., Pires, I. M., Lecane, P. S., Giaccia, A. J., and Hammond, E. M. (2009) *Mol. Cell. Biol.* **29,** 526–537
18. Rappold, I., Iwabuchi, K., Date, T., and Chen, J. (2001) *J. Cell Biol.* **153,** 613–620
19. Zafarullah, M., Li, W. Q., Sylvester, J., and Ahmad, M. (2003) *Cell. Mol. Life Sci.* **60,** 6–20
20. Zhou, B. B., Chaturvedi, P., Spring, K., Scott, S. P., Johanson, R. A., Mishra, R., Mattern, M. R., Winkler, J. D., and Khanna, K. K. (2000) *J. Biol. Chem.* **275,** 10342–10348
21. Hickson, I., Zhao, Y., Richardson, C. J., Green, S. J., Martin, N. M., Orr, A. I., Reaper, P. M., Jackson, S. P., Curtin, N. J., and Smith, G. C. (2004) *Cancer Res.* **64,** 9152–9159
22. von Zglinicki, T., Saretzki, G., Ladhoff, J., d'Adda di Fagagna, F., and Jackson, S. P. (2005) *Mech. Ageing Dev.* **126,** 111–117
23. Brown, J. P., Wei, W., and Sedivy, J. M. (1997) *Science* **277,** 831–834
24. Kang, J. Y., Kim, J. J., Jang, S. Y., and Bae, Y. S. (2009) *Mol. Cells* **28,** 489–494
25. Dimri, G. P., Lee, X., Basile, G., Acosta, M., Scott, G., Roskelley, C., Medrano, E. E., Linskens, M., Rubelj, I., Pereira-Smith, O., Peacocke, M., and Campisi, J. (1995) *Proc. Natl. Acad. Sci. U.S.A.* **92,** 9363–9367
26. Yokoi, T., Fukuo, K., Yasuda, O., Hotta, M., Miyazaki, J., Takemura, Y., Kawamoto, H., Ichijo, H., and Ogihara, T. (2006) *Diabetes* **55,** 1660–1665
27. Finkel, T., and Holbrook, N. J. (2000) *Nature* **408,** 239–247
28. Davies, K. J. (2000) *IUBMB Life* **50,** 279–289
29. Halaby, M. J., Hibma, J. C., He, J., and Yang, D. Q. (2008) *Cell. Signal.* **20,** 1555–1563
30. Suzuki, T., Nishi, T., Nagino, T., Sasaki, K., Aizawa, K., Kada, N., Sawaki, D., Munemasa, Y., Matsumura, T., Muto, S., Sata, M., Miyagawa, K., Horikoshi, M., and Nagai, R. (2007) *J. Biol. Chem.* **282,** 9895–9901
31. Swift, M., and Chase, C. (1983) *Lancet* **1,** 1049–1050.

Cell Stem Cell
Brief Report

Generation of Induced Pluripotent Stem Cells from Human Terminally Differentiated Circulating T Cells

Tomohisa Seki,[1,7] Shinsuke Yuasa,[1,2,7] Mayumi Oda,[2] Toru Egashira,[1] Kojiro Yae,[1] Dai Kusumoto,[1] Hikari Nakata,[1] Shugo Tohyama,[1] Hisayuki Hashimoto,[1] Masaki Kodaira,[1] Yohei Okada,[2,3] Hiroyuki Seimiya,[4] Noemi Fusaki,[5,6] Mamoru Hasegawa,[5] and Keiichi Fukuda[1,*]
[1]Department of Cardiology
[2]Center for Integrated Medical Research
[3]Department of Physiology
Keio University School of Medicine, Tokyo 160-8582, Japan
[4]Division of Molecular Biotherapy, Cancer Chemotherapy Center, Japanese Foundation for Cancer Research, Tokyo 135-8550, Japan
[5]DNAVEC Corporation, Ibaraki 1-25-11, Japan
[6]PRESTO, JST, Saitama 332-0012, Japan
[7]These authors contributed equally to this work
*Correspondence: kfukuda@sc.itc.keio.ac.jp
DOI 10.1016/j.stem.2010.06.003

The direct reprogramming of somatic cells to produce induced pluripotent stem cells (iPSCs) is a prominent recent advance in stem cell biology (Takahashi and Yamanaka, 2006). Generation of iPSCs without genomic integration of extrinsic genes is highly desirable. Initially, human dermal fibroblasts were used to derive human iPSCs (hiPSCs) (Takahashi et al., 2007; Yu et al., 2007). However, recent studies have shown that other human somatic stem cells can be used (Aasen et al., 2008; Eminli et al., 2009; Kim et al., 2009; Ye et al., 2009). It is difficult to obtain human somatic stem cells, but human terminally differentiated circulating T cells (hTDCTCs) are readily available from peripheral blood. Here, we show that a combination of activated T cell cultivation and a temperature-sensitive mutated Sendai virus (SeV) that encodes human OCT3/4, SOX2, KLF4, and c-MYC allows the generation of hiPSCs easily, efficiently, and safely within a 1 month time frame.

Sampling of peripheral blood is one of the least invasive procedures performed routinely in clinics, and surplus peripheral blood samples are often left unused after clinical examinations. Among peripheral blood mononuclear cells (PBMCs), T cells can be readily cultured in vitro by means of a plate-bound anti-CD3 monoclonal antibody and recombinant (r)IL-2 (Desai-Mehta et al., 1996), and we used such an approach to expand hTDCTCs from peripheral blood samples. From 1 ml of whole blood, PBMCs were separated on a Ficoll gradient and then cultured with plate-bound anti-CD3 monoclonal antibody and rIL-2 (Figure 1A). Although PBMC fractions contain lymphocytes and monocytes, T cells are selectively cultured under these conditions. In culture, the number of activated T cells increased gradually but consistently. Five days after blood sampling, the cultured cells were morphologically identical to pure CD3-positive T cells collected by fluorescence-activated cell sorting (FACS) (Figure 1B). We used a whole-PBMC culture method because it is technically simpler than FACS, in which the sorted cells are frequently damaged by laser emission and the process of single-cell sorting.

To avoid transgene integration during iPSC generation, we used an SeV vector, which is a minus-strand RNA virus that is not integrated into the host genome and is not pathogenic for humans (Li et al., 2000). We used a temperature-sensitive mutated SeV vector in these experiments to reduce transgene expression and SeV residue in generated lines. This form of SeV vector generates weaker transgene expression and cannot proliferate at standard culture temperatures (data not shown). SeV can be efficiently transduced into human T cells and can express exogenous genes (Okano et al., 2003). We first introduced green fluorescent protein (GFP) into human T cells by SeV in a dose-dependent manner; toxicity for the infected cells was minimal at the virus dosages used (Figure 1C). To generate iPSCs from hTDCTCs, we used SeV to deliver multiple transgenes that encoded stem cell-specific transcription factors, such as *OCT3/4*, *SOX2*, *KLF4*, and *c-MYC*, into cells on day 6 of culture. Two days after gene introduction, the cells were replated onto feeder layers of SNL cells. On day 9, the cells were transferred to human ES cell (ESC) medium that contained 4 ng/ml bFGF. Within 3 weeks of infection, we identified a colony that resembled human ESCs (hESCs) among the T cell derivatives. On day 25, colonies that were larger and morphologically similar to hESC-like colonies were picked (Figure 1D). Of these initial colonies, which were identified by crystal violet staining, most were positive for alkaline phosphatase (ALP), which is a characteristic marker of stem cells (Figure 1E). T cells that had been transfected with SeV vectors carrying *OCT3/4, SOX2, KLF4,* and *c-MYC* were plated onto mitomycin C-treated SNL feeder cells at 5×10^4 cells per 10 cm dish. Around day 25 after blood sampling, the number of ALP-positive hESC-like colonies was counted and approximately 50 colonies were observed at MOI 20 (Figure 1E) (an efficiency of 0.1%). Moreover, the efficiency of iPSC colony generation was dependent upon the dosage of virus used for gene introduction (Figure 1F). We named these established T cell-derived iPSCs as "TiPS cells (TiPSCs)." After expansion, the cloned TiPSCs displayed typical hESC/iPSC morphology and had a normal karyotype (Figures S1A and S1B available online).

To confirm that the TiPSCs had the characteristics of typical ESC/iPSCs, we

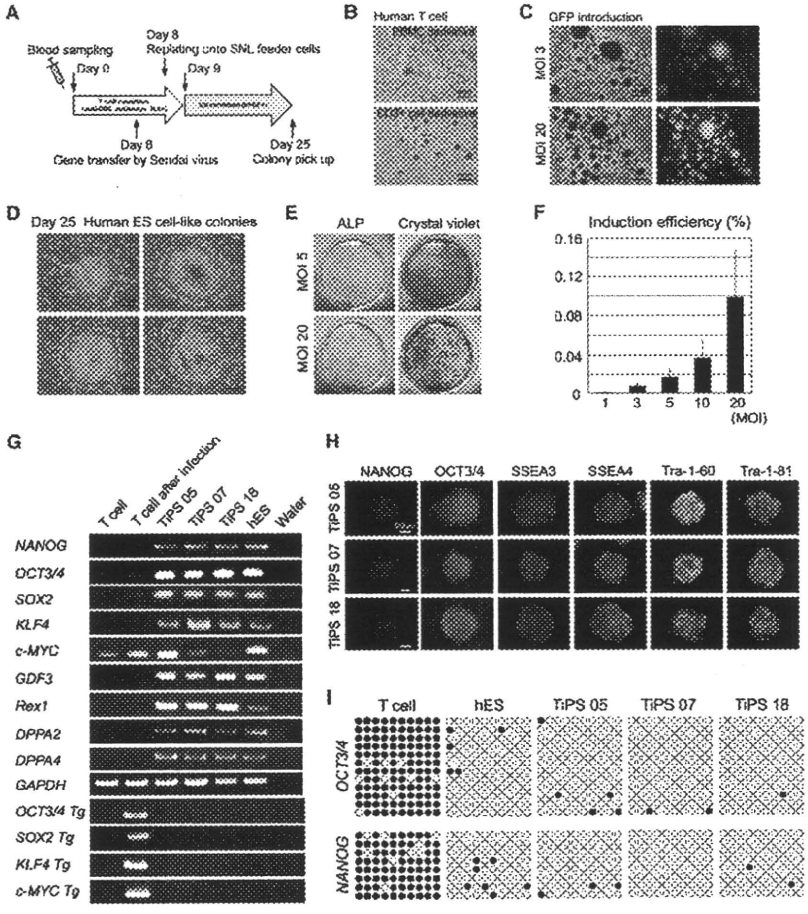

Figure 1. hTDCTCs-Derived iPSC Colonies

(A) Strategy used in the present study for reprogramming T cells.

(B) Morphologies of T cells derived from whole PBMCs or FACS-sorted T cells grown in the presence of CD3 antibody and rIL2.

(C) Efficient GFP introduction by SeV in T cells transfected at an MOI of 3 or MOI of 20.

(D) Typical ESC-like iPSC colonies on day 25 after blood sampling.

(E) Examples of 10 cm dishes stained for ALP on day 25, showing numerous ALP-positive colonies of T cells that were transfected at an MOI of 5 or MOI of 20.

(F) Numbers of ALP-positive colonies in relation to multiplicity of infection.

(G) RT-PCR analyses for the hESC marker genes *NANOG*, *OCT3/4*, *SOX2*, *KLF4*, *c-MYC*, *GDF3*, *REX1*, *DPPA2*, and *DPPA4* and the transgenes *OCT3/4*, *SOX2*, *KLF4*, and *c-MYC*.

(H) Immunofluorescence staining for pluripotency and surface markers (NANOG, OCT3/4, SSEA3, SSEA4, TRA-1-60, and TRA-1-81) in TiPS 05, 07, and 18. Scale bars represent 500 μm.

(I) Bisulfite sequencing analysis of the *NANOG* and *OCT3/4* promoter regions in peripheral T cells, hESCs, and hTiPSCs 05, 07, and 18. Each row of circles for a given amplicon represents the methylation status of the CpG dinucleotides in one bacterial clone for that region. Open circles represent unmethylated CpGs; closed circles represent methylated CpGs.

See also Figure S1 and Table S1.

examined stem cell marker expression. Reverse-transcription PCR (RT-PCR) analyses revealed that the TiPS 05, 07, and 18 clones expressed ESC marker transcripts for *NANOG*, *OCT3/4*, *SOX2*, *KLF4*, *c-MYC*, *GDF3*, *REX1*, *DPPA2*, and *DPPA4*. The original T cells also expressed *c-MYC* at a basal level, as previously reported (Douglas et al., 2001). In the TiPSCs, the *OCT3/4*, *SOX2*, *KLF4*, and *c-MYC* transgenes were lost after several passages (Figure 1G; Figure S1C). Immunostaining revealed that the TiPSCs expressed the Nanog, Oct3/4, SSEA3, SSEA4, Tra-1-60, and Tra-1-81 proteins (Figure 1H). High telomerase activity is also an important characteristic of iPSCs, and, appropriately, TiPSCs showed high levels of telomerase activity (Figure S1D). Another signature of iPSCs is epigenetic remodeling. We used bisulfite sequencing to examine the methylation status of the *NANOG* and *OCT3/4* promoters. T cells, which do not express *NANOG* or *OCT3/4*, showed mostly methylated CpGs in those promoters. hESCs, which do express *NANOG* and *OCT3/4*, showed unmethylated CpGs in those promoters. As in hESCs, the CpGs in these promoter regions were predominantly unmethylated in the TiPSCs (Figure 1I). These results suggest that SeV-mediated gene transfer successfully reprograms hTDCTCs.

Somatic recombination of T cell receptor (TCR) genes generates a diverse T cell repertoire that allows adaptation for antigen responses (Krangel, 2009). To confirm that the TiPSCs were derived from hTDCTCs, we analyzed TCR rearrangements. A hallmark of the TCR-β locus is developmentally ordered recombination, with Dβ-to-Jβ recombination preceding Vβ-to-DβJβ recombination. We performed capillary electrophoresis of the PCR products for the genomic DNA of the TCR-β regions. As a positive control, we used monoclonal T cells, which are derived from patients with lymphocyte malignancies and show a specific peak, because these T cells have only a single genetic variation in their TCR regions (Figure S2A). Peripheral T cells from people without lymphocytic diseases are polyclonal, with diverse genetic variations in their TCR rearrangements, and show a broad and low band without a specific peak. ESCs do not have TCR rearrangements and do not show a specific positive peak. The TiPS 05, 07, and 18 cell lines showed specific peaks for Dβ/Jβ recombination. TiPS 05 showed Vβ/Jβ2 recombination. TiPS 07 and TiPS 18 showed Vβ/Jβ1,2 recombination, albeit with different bands (Figure 2A). TCR rearrangement is specific for T cell development, so these results confirm that TiPSCs are derived from T cells. They also indicate that the TiPS 05, 07, and 18 lines originated from different T cells. We analyzed the rearrangement pattern of 10 independent TiPSCs and confirmed that every TiPSCs showed different rearrangement pattern (Figure S2A).

We also performed global gene expression analyses with DNA chips. Scatter plot analyses revealed global gene

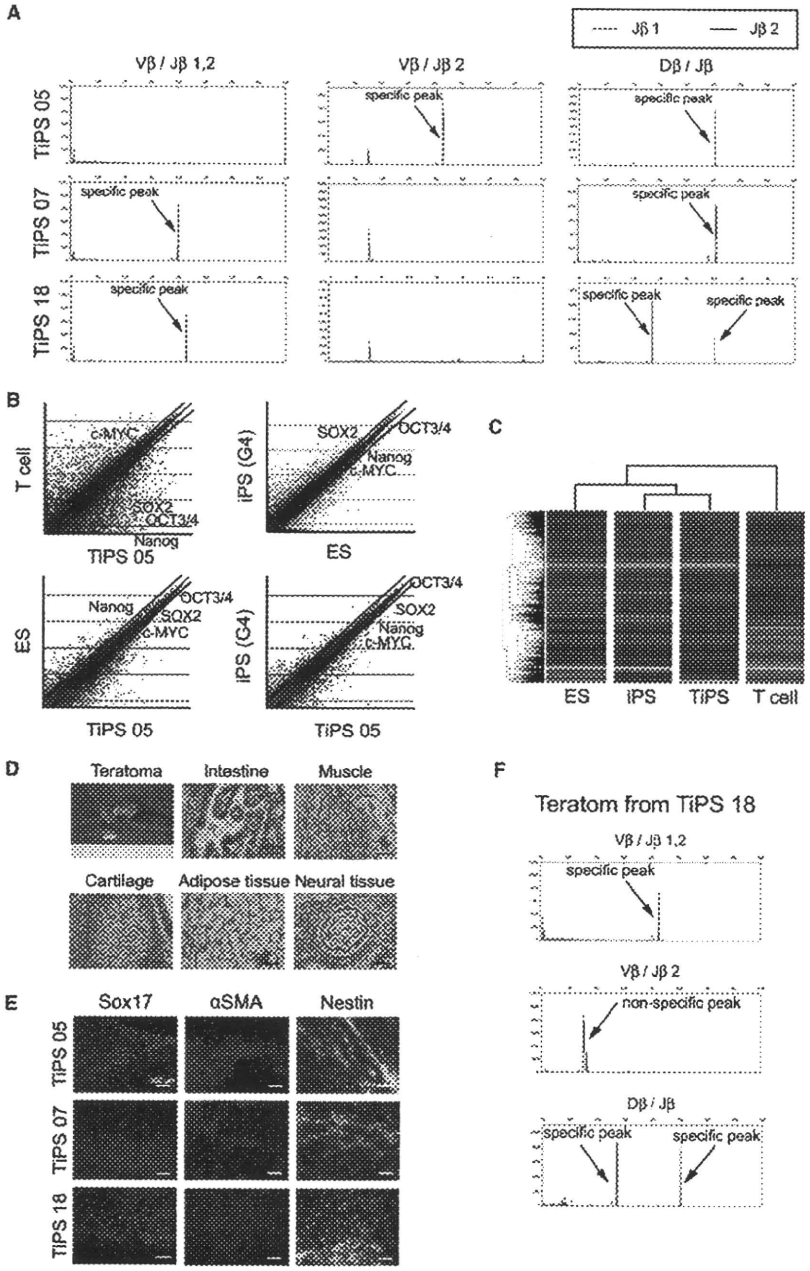

Figure 2. Detail Characterizations of TiPSCs

(A) Characterization of the TCR-β rearrangement by capillary electrophoresis. The green line is derived from the band for the Jβ1 gene, and blue line is derived from the band for the Jβ2 gene. TiPS 05 shows rearrangements of Vβ/Jβ2 and Dβ/Jβ. TiPS 07 shows rearrangements of Vβ/Jβ1,2 and Dβ/Jβ. TiPS 18 shows rearrangements of Vβ/Jβ1,2 and Dβ/Jβ.

(B) Scatter plots comparing the global gene expression profiles of T cells and TiPS cells, dermal fibroblast-derived iPSCs (G4) and ESCs, ESCs and TiPSCs, and dermal fibroblast-derived iPSCs (G4) and TiPSCs. The black lines indicate 2-fold differences in gene expression levels between the paired cell populations. The transcript expression levels are shown on a $\log_2$ scale. The expression levels of *NANOG*, *OCT3/4*, *SOX2*, and *c-MYC* are shown.

(C) Heat map analyses of hESCs, dermal fibroblast-derived iPSCs, TiPSCs, and the parental human T cells.

(D) Gross morphology, hematoxylin and eosin-stained representative teratomas derived from TiPS 05.

(E) Immunofluorescence staining for Sox17 (endodermal marker), αSMA (mesodermal marker), and Nestin (ectodermal marker) in each TiPSC-derived differentiated cell.

(F) Characterization of the TCR-β rearrangement for teratoma from TiPS 18.

See also Figure S2 and Table S2.

expression differences between peripheral T cells and TiPSCs. Comparison of hESCs and human dermal fibroblast-derived iPSCs, hESCs, and human TiPSCs (hTiPSCs), and dermal fibroblast-derived iPSCs and TiPSCs showed high levels of similarity (Figure 2B). Heat map analysis showed that the global gene expression profiles were overall similar in ESCs, dermal fibroblast-derived iPSCs, and TiPSCs, and different from T cells (Figure 2C). To further demonstrate the pluripotency of hTiPSCs, they were transplanted into the subcutaneous tissue of severe combined immunodeficient (SCID) mice. Six to eight weeks after injection, each TiPSC line tested gave rise to teratomas that contained derivatives of all three germ layers (Figure 2D; Figure S2B). We also examined the in vitro differentiation potential of TiPSCs. Each TiPSC line tested generated embryoid bodies that contained derivatives of all three germ layers (Figure 2E). These results indicate that hTiPSCs are pluripotent stem cells. Although it was reported that Trp53 null murine T cells could be reprogrammed into iPSCs (Hong et al., 2009), we have successfully reprogrammed wild-type human T cells. In our hands, the efficiency of conventional retrovirus-mediated gene transfer into wild-type human T cells was very low compared to SeV (data not shown). In our view, the efficiency of gene transfer is a major determining factor in successful iPSC generation.

With current technology, if iPSC-derived mature cells are transplanted into diseased patients, there is no good procedure for following their progeny, which could eventually form malignant or benign tumors. In animal models, several marker genes can be used to chart the progression and consequences of iPSC-derived mature cell transplantation, such as GFP and luciferase. However, it is not desirable to insert exogenous marker genes into the genomes of hiPSCs for clinical use. TiPSCs, however, already have a traceable genetic signature through TCR locus rearrangement. Consistent with this idea, teratomas derived from TiPSCs had

same signature as undifferentiated TiPSCs (Figure 2F; Figure S2C). Therefore, the descendents of TiPSCs can be identified by analyzing their TCR rearrangement patterns.

In conclusion, we have developed a minimally invasive method for hiPSC generation without genomic integration that uses low numbers of hTDCTCs from peripheral blood. This method has advantages for research into stem cell reprogramming, TCR rearrangement, immunologic disorders, and the development of genetic markers for future applications of regenerative medicine. TiPSCs may well be relatively easy to use in a clinical setting.

ACCESSION NUMBERS

The microarray data have been deposited in GEO and given the series accession number GSE22088.

SUPPLEMENTAL INFORMATION

Supplemental Information includes Supplemental Experimental Procedures, two figures, and two tables and can be found with this article online at doi:10.1016/j.stem.2010.06.003.

ACKNOWLEDGMENTS

This study was supported in part by research grants from the project for realization of regenerative medicine, the Ministry of Education, Science, and Culture, Japan, and by a grant from the New Energy and Industrial Technology Development Organization (NEDO). We thank Dr. Kyotaro Hirashima for technical assistance with TRAP assay. N.F. is an employee of DNAVEC Corporation and M.H. is a founder and shareholder of DNAVEC Corporation

Received: May 5, 2010
Revised: June 3, 2010
Accepted: June 5, 2010
Published: July 1, 2010

REFERENCES

Aasen, T., Raya, A., Barrero, M.J., Garreta, E., Consiglio, A., Gonzalez, F., Vassena, R., Bilic, J., Pekarik, V., Tiscornia, G., et al. (2008). Nat. Biotechnol. *26*, 1276–1284.

Desai-Mehta, A., Lu, L., Ramsey-Goldman, R., and Datta, S.K. (1996). J. Clin. Invest. *97*, 2063–2073.

Douglas, N.C., Jacobs, H., Bothwell, A.L., and Hayday, A.C. (2001). Nat. Immunol. *2*, 307–315.

Eminli, S., Foudi, A., Stadtfeld, M., Maherali, N., Ahfeldt, T., Mostoslavsky, G., Hock, H., and Hochedlinger, K. (2009). Nat. Genet. *41*, 968–976.

Hong, H., Takahashi, K., Ichisaka, T., Aoi, T., Kanagawa, O., Nakagawa, M., Okita, K., and Yamanaka, S. (2009). Nature *460*, 1132–1135.

Kim, J.B., Greber, B., Arauzo-Bravo, M.J., Meyer, J., Park, K.I., Zaehres, H., and Scholer, H.R. (2009). Nature *461*, 649–653.

Krangel, M.S. (2009). Curr. Opin. Immunol. *21*, 133–139.

Li, H.-O., Zhu, Y.-F., Asakawa, M., Kuma, H., Hirata, T., Ueda, Y., Lee, Y.-S., Fukumura, M., Iida, A., Kato, A., et al. (2000). J. Virol. *74*, 6564–6569.

Okano, S., Yonemitsu, Y., Nagata, S., Sata, S., Onimaru, M., Nakagawa, K., Tomita, Y., Kishihara, K., Hashimoto, S., Nakashima, Y., et al. (2003). Gene Ther. *10*, 1381–1391.

Takahashi, K., and Yamanaka, S. (2006). Cell *126*, 663–676.

Takahashi, K., Tanabe, K., Ohnuki, M., Narita, M., Ichisaka, T., Tomoda, K., and Yamanaka, S. (2007). Cell *131*, 861–872.

Ye, Z., Zhan, H., Mali, P., Dowey, S., Williams, D.M., Jang, Y.-Y., Dang, C.V., Spivak, J.L., Moliterno, A.R., and Cheng, L. (2009). Blood *114*, 5473–5480.

Yu, J., Vodyanik, M.A., Smuga-Otto, K., Antosiewicz-Bourget, J., Frane, J.L., Tian, S., Nie, J., Jonsdottir, G.A., Ruotti, V., Stewart, R., et al. (2007). Science *318*, 1917–1920.

Note Added in Proof

A manuscript has appeared online demonstrating isolation of iPSCs from peripheral blood, including a single line that showed evidence for both TCR-β and TCR-γ rearrangement by PCR (Kunisato, A., Wakatsuki, M., Shinba, H., Ota, T., Ishida, I., and Nagao, K. [2010]. Direct generation of induced pluripotent stem cells from human non-mobilized blood. Stem Cells Dev., in press. Published online May 24, 2010. 10.1089/scd.2010.0063).

Cardiovascular Research (2011) 89, 309–319
doi:10.1093/cvr/cvq335

Adiponectin protects against doxorubicin-induced cardiomyopathy by anti-apoptotic effects through AMPK up-regulation

Masanori Konishi[1], Go Haraguchi[1], Hirokazu Ohigashi[1], Takashi Ishihara[1], Kiyomi Saito[2], Yasuko Nakano[3], and Mitsuaki Isobe[1]*

[1]Department of Cardiovascular Medicine, Tokyo Medical and Dental University, 1-5-45 Yushima, Bunkyo-ku, Tokyo 113-8519, Japan; [2]Center for Biotechnology, Showa University, Tokyo, Japan; and [3]Department of Pharmacogenomics, School of Pharmaceutical Sciences, Showa University, Tokyo, Japan

Received 26 May 2010; revised 20 September 2010; accepted 20 October 2010; online publish-ahead-of-print 25 October 2010

Time for primary review: 33 days

Aims Adiponectin (APN) has been reported to protect against ischaemia–reperfusion injury and hypertrophy. However, few reports have investigated the cardioprotective effects of APN in doxorubicin (DOX)-induced cardiomyopathy; therefore, we studied the cardioprotective mechanisms of APN in this model.

Methods and results In an *in vivo* study, we quantified the cardiac pathohistology of C57BL/6 mice [wild-type (WT) mice], APN transgenic mice with high APN concentrations [APN transgenic sense (SE) mice], and those with reduced APN concentrations [APN transgenic antisense (AS) mice] after intraperitoneal injections of DOX (4 mg/kg) weekly for 6 weeks. The survival rate after 14 days was significantly increased in APN-SE mice (WT vs. APN-AS vs. APN-SE: 40 vs. 17 vs. 73%, $P < 0.05$). We assessed myocardial pathohistological changes and observed that fibrosis and apoptosis were significantly decreased in APN-SE mice compared with those of the other groups. We also assessed DOX-induced apoptotic mechanisms *in vitro* using cultured cardiomyocytes isolated from neonatal WT mice. The expression of adenosine monophosphate-activated protein kinase (AMPK) and anti-apoptotic factor Bcl-2 increased, but that of pro-apoptotic factor Bax decreased in cardiomyocytes treated with highly concentrated APN. The protective effects of APN were reversed by the addition of an AMPK inhibitor (dorsomorphin) to the culture medium.

Conclusion These data suggest that APN improved cardiac function through anti-apoptotic effects by up-regulation of AMPK in DOX-induced cardiomyopathy in mice.

Keywords Apoptosis • Cardiomyopathy • Heart failure

1. Introduction

Adiponectin (APN) is an adipocyte-derived bioactive factor that is abundantly present in the human plasma.[1] It exists in human and mouse plasma in the form of the following oligomers: trimer, hexamer, and high-molecular-weight oligomer.[2] APN works as a major anti-diabetic and anti-atherogenic adipokine. APN receptors 1 and 2 (AdipoR1 and AdipoR2) have been proved to mediate anti-diabetic effects.[3] Circulating APN levels are diminished in obese individuals[1] and type 2 diabetes patients.[4] Previous studies have been unable to ascertain whether high plasma APN levels have cardioprotective properties in heart failure (HF) patients. Some studies have found that high APN levels are associated with increased mortality in HF patients,[5,6] perhaps because high APN levels are indicative of systemic wasting in these populations.[1] In this regard, low body mass index (BMI), which leads to elevated APN levels, is associated with increased mortality following the onset of HF, whereas elevated BMI, which leads to reduced APN levels, increases the risk of HF.[7] In contrast, high APN levels have been associated with a lower risk of myocardial infarction (MI),[8] whereas a rapid decline in APN levels following MI and persistently low APN levels could be predictive of future adverse cardiac events following MI.[9] Furthermore, low APN levels have been associated with progression of left ventricular (LV) hypertrophy in hypertensive patients.[10] In experimental studies, APN-

* Corresponding author. Tel: +81 3 5803 5951; fax: +81 3 5803 0238, Email: isobemi.cvm@tmd.ac.jp

knockout (APN-KO) mice exhibited diet-induced insulin resistance,[11] impaired angiogenic response to ischaemia through the suppression of excess reactive oxygen species production,[12] and excessive cardiac remodelling after pressure overload via the suppression of extracellular signal-regulated kinase activities.[13] Furthermore, APN increased adenosine monophosphate-activated protein kinase (AMPK) activities in cardiomyocytes, thus preventing cardiac dysfunction.[14]

Although doxorubicin (DOX) is a very effective anti-neoplastic agent with a broad antitumour spectrum, its clinical use is limited by progressive and dose-related cardiotoxicity that may not manifest itself until many years after treatment.[15] Two distinct phases of DOX-induced cardiotoxicity have been described: acute cardiotoxicity and chronic cardiomyopathy.[16] The former typically occurs within several weeks of DOX administration and is characterized by acute inflammation. The latter appears as many as 15 years after DOX administration and is characterized by progressive LV dysfunction leading to irreversible congestive HF.[17] DOX-induced HF has been attributed to apoptosis mediated by the intrinsic signalling cascade, resulting in mitochondrial dysfunction and myofibrillar degeneration.[18] In animal models, studies have shown that DOX causes apoptotic cell death in cardiomyocytes.[19] We also reported that exogenous nitric oxide produced an anti-apoptotic effect by suppressing caspase activity via S-nitrosylation in DOX-induced cardiomyopathy.[20] Furthermore, it has been shown that the suppression of AMPK and its phosphorylation results in increased apoptosis of cardiomyocytes in DOX-induced cardiomyopathy.[21]

Although investigation of the mechanism of anti-apoptosis in cardiomyocytes could lead to new treatments for HF, there are currently no reports on whether APN has cardioprotective effects in DOX-induced chronic cardiomyopathy. Here, we investigated the roles of APN and APN-associated signals in DOX-induced chronic cardiomyopathy in APN transgenic mice. We also assessed the mechanisms of the cardioprotective effects of APN in this model.

2. Methods

2.1 Generation of transgenic mice

We used the same transgenic mice as described previously.[22] Sense and antisense APN expression vectors were constructed by insertion of an inverted fragment of mouse APN complementary DNA into the unique *Eco*RI site. A Basic Local Alignment Search Tool (BLAST) analysis (National Center for Biotechnology Information, National Library of Medicine, Bethesda, MD, USA) of the GenBank nucleotide database indicated that these sequences showed no significant homology to any other mouse genes.

2.2 Animals and experimental protocol

APN transgenic sense (APN-SE) mice ($n = 30$), APN transgenic antisense (APN-AS) mice ($n = 30$), and C57BL/6 mice as wild-type (WT) controls ($n = 30$) received an intraperitoneal injection of either DOX (Wako Pure Chemical, Osaka, Japan) or saline at 8 weeks of age. DOX was dissolved in sterile saline immediately before use and injected at a volume of 30 μL and a concentration of 4 mg/kg once a week for 6 weeks. The control animals were injected with an equivalent volume of saline. The animals were observed daily and weighed weekly. After 14 days from the last injection, the cardiac functions of the animals were examined by the usual methods and the animals were then sacrificed. This previously described model reproducibly introduced end-stage HF.[23] All animals were maintained in accordance with the Guide for the Care and Use of Laboratory Animals published by the US National Institutes of Health (NIH Publication No. 85-23, revised 1996). The protocol was approved by the Animal Research Committee of Tokyo Medical and Dental University.

2.3 Physiological studies

Blood pressure (BP) and heart rate were measured using a tail-cuff system on unanaesthetized mice that had been pre-warmed for 10 min at 37°C in a thermostatically controlled heating cabinet (BP-98A; Softron, Tokyo, Japan). Transthoracic echocardiography was carried out with an ultrasound machine (Nemio; Toshiba, Tokyo, Japan) and a 13 MHz annular array transducer under light chloral hydrate anaesthesia (10 mg/kg) (Wako Pure Chemical Ind.). Hearts were imaged in two-dimensional mode in short-axis views at the level of the papillary muscles. Interventricular septal thickness (IVST), posterior wall thickness, LV end-diastolic dimension (LVDd), LV end-systolic dimension (LVDs), and the fractional shortening ratios {% FS = [(LVDd − LVDs)/LVDd] × 100} were calculated from the M-mode recordings. Each dimension was presented as the average of measurements recorded over three consecutive cardiac cycles. Measurements were made offline by two independent investigators.

2.4 Histological analysis

Hearts were removed immediately after sacrifice and fixed in 10% phosphate-buffered formalin. The fixed tissue was then embedded in paraffin and cut transversely into sections. These sections were stained with haematoxylin–eosin (HE) and Masson's trichrome staining (Muto Pure Chemicals, Tokyo, Japan). The area of the myocardium and surrounding tissue affected by the myocarditis (consisting of inflammatory cells and myocardial necrosis) was determined by computer-assisted analysis (Scion Image beta 4.0.2; Scion Corp., Frederick, MD, USA). For the analysis of LV fibrosis, six random photomicrographs were taken of the viable myocardium for each animal. The fibrosis extent and myocyte diameter in these photomicrographs was quantified by a blinded observer using the ImageJ program from NIH Image Software (National Institutes of Health, Bethesda, MD, USA). All data were analysed in a blind fashion by two independent investigators and then averaged.

2.5 Cell culture and treatment

Neonatal cardiomyocytes from 1- or 2-day-old WT mice were isolated, subjected to Percoll gradient centrifugation, and cultured *in vitro* as described previously.[20] The cardiomyocytes were incubated in Eagle's minimum essential medium (Sigma Chemical Co., St Louis, MO, USA) supplemented with 5% calf serum (JRH Biosciences, Lenexa, KS, USA) for 24 h at 37°C.[24] The cardiomyocytes were divided into five groups: the saline group ($n = 6$), in which only 4 μL of saline was added to the cultured medium and 1 μmol/L DOX was added to induce myocardial apoptosis after 12 h; the medium-concentrated APN (APN-medium) group ($n = 6$), in which 30 μg/mL APN (BioVendor Research and Diagnostic Products, Candler, NC, USA) was added and 1 μmol/L DOX was added; the high-concentrated APN (APN-high) group ($n = 6$), in which 100 μg/mL APN and 1 μmol/L DOX were added; the AMPK inhibitor (APN-high + AMPK-I) group ($n = 6$), in which a 90 min pre-treatment with an AMPK inhibitor, Compound **C** (dorsomorphin),[25] 6-[4-(2-piperidin-1-yl-ethoxy)-phenyl]-3-pyridin-4-yl-phyrrazolo[1,5-*a*]-pyrimidine (Calbiochem, La Jolla, CA, USA), inhibited AMPK phosphorylation, after which time 100 μg/mL APN and 1 μmol/L DOX were added; and the AMPK activator [saline + 5-aminoimidazole-4-carboxyamide ribonucleoside (AICAR)] group ($n = 6$), in which a 90 min pre-treatment with an AMPK activator, AICAR[26] (Cell Signaling Technology, Danvers, MA,

Table 1 Primer sequences for RT–PCR analysis

Gene	Number	Primer sequences (5′–3′)		Amplicon size (bp)
		Forward	Reverse	
AdipoR1	BC014875	ACGTTGGAGAGTCATCCCGTAT	CTCTGTGTGGATGCGGAAGAT	136
AdipoR2	BC064109	TCCCAGGAAGATGAAGGGTTTAT	TTCCATTCGTTCGATAGCATGA	75
AMPK-α1	AY885266	TGAGAACGTCCTGCTTGATG	GACTTTCTGGTGCGGCATAAT	128
AMPK-α2	BC138565	GCTGTGGATCGCCAAATTAT	CACGTGCTCATCATCGAAAG	120
Bcl-2	BC095964	CCTGTGGATGACTGAGTACC	GAGACAGCCAGGAGAAAT	128
Bax	BC053380	GGTGGCAGCTGACATGTTTG	GCCTTGAGCACCAGTTTGC	90
GAPDH	BC096590	TGCACCACCAACTGCTTA	GGATGCAGGGATGATGTTC	177

All primers used in this study are shown.

USA), activated the phosphorylation of AMPK, after which time 4 μL of saline and 1 μmol/L DOX were added. Each group of control cardiomyocytes were injected with an equivalent volume of saline, without DOX. After 24 h from the last addition of saline or DOX, the cardiomyocytes were harvested from the cultured medium. For the investigation of mitochondria-dependent death pathways, mitochondria were isolated from the cardiomyocytes using a commercially available kit (Pierce Biotechnology, Inc., Rockford, IL, USA) in accordance with the manufacturer's instructions.

2.6 Quantitative reverse transcription–polymerase chain reaction

Total RNA was extracted from cultured cardiomyocytes using Trizol reagent and purified using RNeasy columns (Qiagen, Valencia, CA, USA), and 1 μg of DNAase-treated total RNA was reverse transcribed using First-Strand Beads (Applied Biosystems, Tokyo, Japan) with random primers. All oligonucleotide primers for polymerase chain reaction (PCR) were designed with Primer Express software and synthesized by Sigma-Genosys Japan (Tokyo, Japan) (*Table 1*). The PCRs were performed with iQ SYBR Green Supermix (Bio-Rad Laboratories, Hercules, CA, USA) on a Light Cycler instrument (Roche Diagnostics, Meylan, France). Expression of the target genes was measured in triplicate and then normalized to the level of the housekeeping gene glyceraldehyde-3-phosphate dehydrogenase (GAPDH).

2.7 Quantification of serum total APN

Serum total APN concentrations were determined using an ELISA kit (R&D Systems, Inc., Minneapolis, MN, USA) in accordance with the manufacturer's instructions.

2.8 Assessment of apoptosis

The percentage of cells undergoing apoptosis was calculated as the ratio of apoptotic cells to total cells. Apoptotic cardiomyocytes detach from the substratum; therefore, the extent of apoptosis can be determined by counting floating and adherent cells using a cell counter (CDA-500; Sysmex, Long Grove, IL, USA).[20] The terminal deoxynucleotidyl transferase-mediated dUTP nick end-labelling (TUNEL) assay was performed according to the manufacturer's instructions using a commercially available kit for detecting end-labelled DNA and anti-digoxigenin-rhodamine (Roche Diagnostics, Mannheim, Germany). The caspase-3 assay was carried out using the CaspACE assay system (Promega, Madison, WI, USA). The cells were harvested and lysed in the cell lysis buffer included with the kit, and the protein concentrations were equalized for each condition. Subsequently, the cell lysate was combined with an equal amount of substrate reaction buffer containing a caspase-3 colorimetric substrate, acetyl-DEVD-*p*-nitroaniline (*p*Na). This mixture was incubated for 2 h at 37°C, and absorbance was measured with a plate reader (Ultramark; Bio-Rad).

2.9 Western blot analysis

Western blotting was performed for cell and tissue lysates using polyclonal antibodies for mouse procaspase-3 (#9662; Cell Signaling Technology, Danvers, MA, USA), cleaved caspase-3 (#9664S), cytochrome *c* (#4272), phosphorylated-AMPK-α [Thr^{172}, a synthetic phosphor-peptide (KLH-coupled) corresponding to residues surrounding Thr^{172} of human AMPK-α, #2531], AMPK-α (#2532), Bcl-2 (#2876), Bax (#2772), voltage-dependent anion channel (#4866), GAPDH (#2118), AdipoR1 (#sc-46748; Santa Cruz Biotechnology, Inc., Santa Cruz, CA, USA), and AdipoR2 (#LS-C34900; LifeSpan Biosciences, Seattle, WA, USA). Bands were detected with an enhanced chemiluminescence reagent (Thermo Scientific Ind., Rockford, IL, USA) on LAS-1000 (Fujifilm, Tokyo, Japan). Densitometric analysis was conducted using the ImageJ program.

2.10 Statistical analyses

All values are reported as means ± standard deviation. Differences were analysed with one-way analysis of variance (ANOVA) and *post hoc* analysis was performed with the Bonferroni/Dunnett test included in the commercially available SPSS software package (SPSS Japan, Tokyo, Japan). The Kaplan–Meier analysis was used to examine survival differences between the groups. Differences were considered significant at $P < 0.05$.

3. Results

3.1 Physiological studies and biomarkers *in vivo*

In all groups, serum total APN levels were significantly lower after 14 days than at the baseline. Those in the APN-SE group were about double those in the WT group. Also, those in the APN-AS group were about half of those in the WT group (*Figure 1A*). At necropsy, we found the following: of the WT group, 10 mice had ascites, four had lobulated enlarged livers indicative of liver congestion, and three had foamy lungs indicative of pulmonary oedema; of the APN-SE group, three had ascites, two had liver congestion, and two

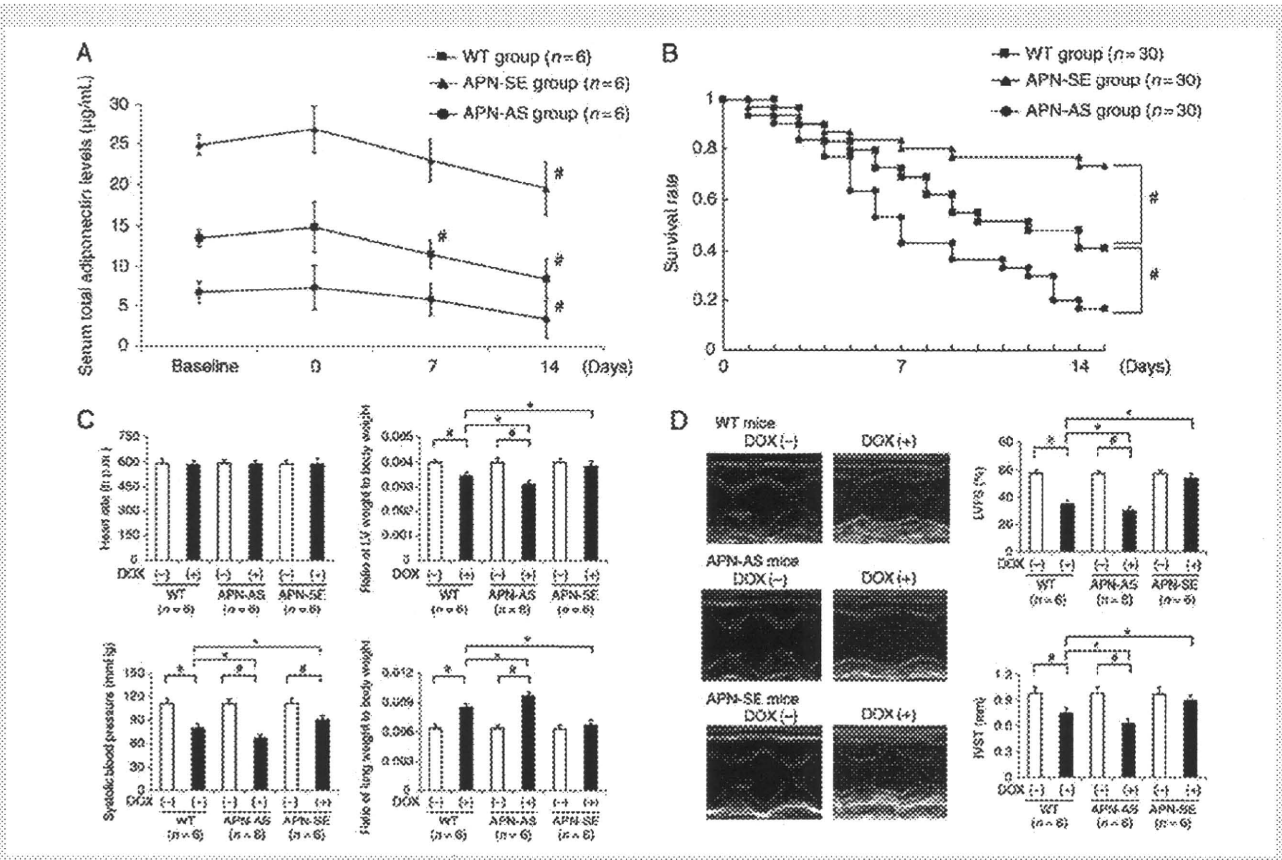

Figure 1 (*A*) Evaluation of serum total APN levels in the WT ($n = 6$), APN-SE ($n = 6$), and APN-AS ($n = 6$) groups. (*B*) Kaplan–Meier curves of survival in the WT ($n = 30$), APN-SE ($n = 30$), and APN-AS ($n = 30$) groups. (*C*) Haemodynamic and morphological parameters after 14 days in the WT ($n = 6$), APN-SE ($n = 6$), and APN-AS ($n = 6$) groups. (*D*) M-mode echocardiographic parameters after 14 days in the WT ($n = 6$), APN-SE ($n = 6$), and APN-AS ($n = 6$) groups. Time is expressed in days after the last DOX injection. $^{\#}P < 0.05$ compared with baseline [in (*A*)]. *P*-value refers to the log-rank analysis. $^{\#}P < 0.05$ compared with the WT group [in (*B*)]. Open bars indicate the vehicle-injected mice of each group; closed bars indicate the DOX-injected mice of each group. $^{\#}P < 0.05$ compared with the vehicle mice of each group. $^{*}P < 0.05$ compared with the WT group after DOX injection [in (*C*) and (*D*)].

had pulmonary oedema; of the APN-AS group, 14 had ascites, six had liver congestion, and four had pulmonary oedema. The survival rate after DOX treatment was significantly higher in the APN-SE group than in the WT group and was significantly lower in the APN-AS group than in the WT group (*Figure 1B*).

In haemodynamic and morphological parameters, heart rates did not significantly differ among the three groups. Systolic BP significantly decreased in DOX-injected mice compared with vehicle-injected mice in all groups. Systolic BP was significantly preserved in the APN-SE group compared with the WT and APN-AS groups. The ratio of LV weight to body weight significantly decreased after DOX injection in the WT and APN-AS groups but was preserved in the APN-SE group. In contrast, the ratio of lung weight to body weight significantly increased after DOX injection in the WT and APN-AS groups but was preserved in the APN-SE group (*Figure 1C*). In echocardiographic studies, LVFS and IVST significantly decreased after DOX injection in the WT and APN-AS groups but were preserved in the APN-SE group (*Figure 1D*). The thickness of the posterior wall showed a similar tendency (data not shown).

3.2 Apoptotic myocardial changes *in vivo*

In HE staining of the myocardium, cardiomyocyte size significantly decreased after DOX injection in the WT and APN-AS groups but was preserved in the APN-SE group. On the other hand, the area of fibrosis seen on Masson's trichrome staining significantly increased in the WT and APN-AS groups compared with the APN-SE group (*Figure 2A*).

Apoptotic cells in the *in vivo* cardiomyocytes detected as TUNEL-positive nuclei significantly increased after DOX injection in the WT and APN-AS groups but did not in the APN-SE group (*Figure 2B*).

3.3 Expression of AdipoR1, AdipoR2, and AMPK *in vivo*

AdipoR1 and AdipoR2 transcripts were significantly down-regulated after DOX injection. However, although AdipoR2 down-regulation was similar between the three groups, AdipoR1 was less down-regulated in the APN-SE group. The messenger RNA (mRNA) expression of AMPK-α1 and -α2 significantly decreased after

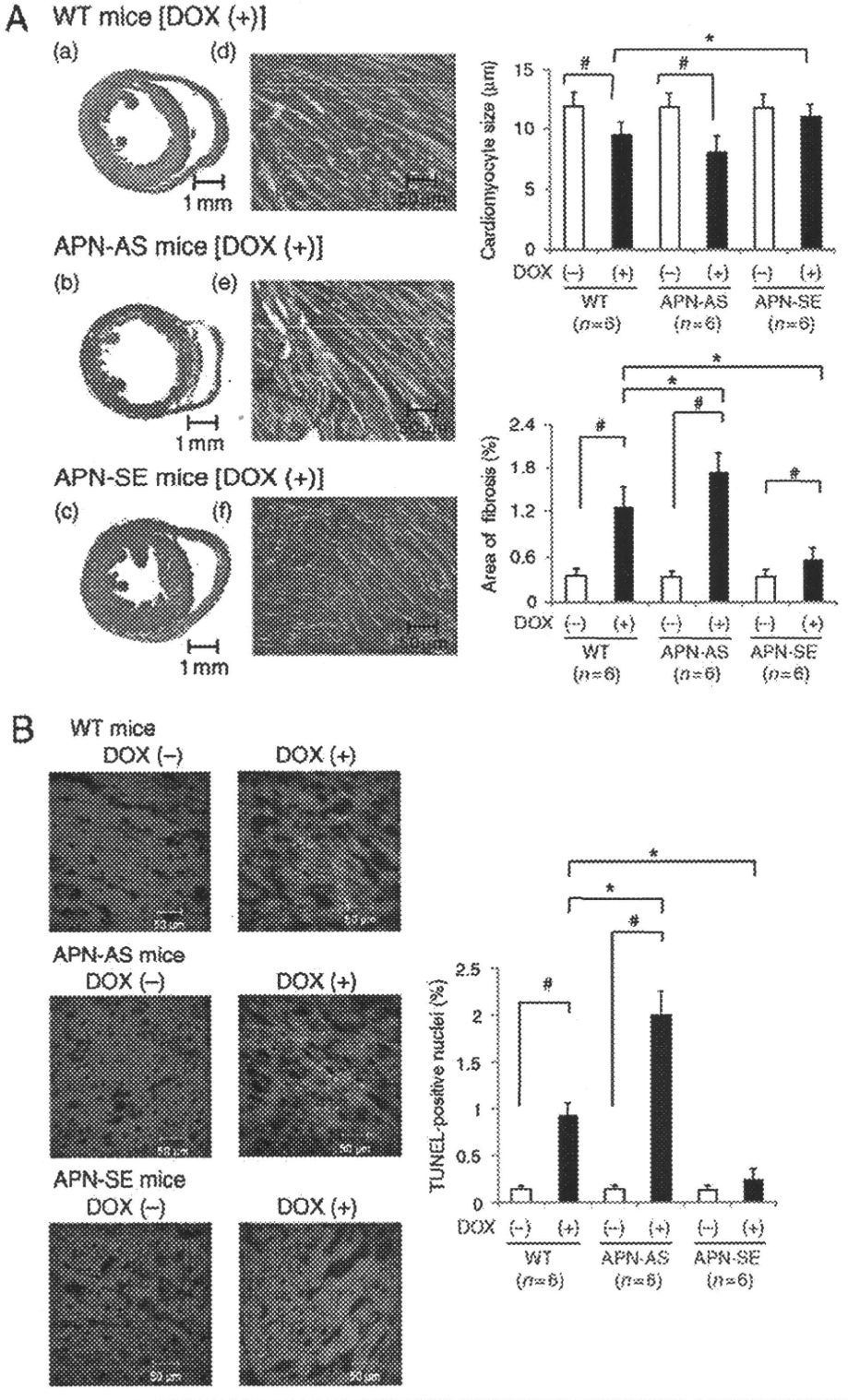

Figure 2 (*A*) Histological changes after 14 days in the WT ($n = 6$), APN-SE ($n = 6$), and APN-AS ($n = 6$) groups. (*a–e*) Masson's trichrome staining. Original magnification in (*a–c*) is ×20. Original magnification in (*d–f*) is ×400. (*B*) Myocardium apoptosis *in vivo* after 14 days in the WT ($n = 6$), APN-SE ($n = 6$), and APN-AS ($n = 6$) groups. Bars, 50 μm. Open bars indicate the vehicle-injected mice of each group; closed bars indicate the DOX-injected mice of each group. $^{\#}P < 0.05$ compared with the vehicle-injected mice of each group. $^{*}P < 0.05$ compared with the WT group after DOX injection.

DOX injection in the WT and APN-AS groups but increased in the APN-SE group. The mRNA expression of Bax significantly increased after DOX injection in the WT and APN-AS groups but was suppressed in the APN-SE group. In contrast, mRNA expression of Bcl-2 significantly decreased after DOX injection in the WT and APN-AS groups but not in the APN-SE group (*Figure 3A*).

In western blotting analyses, the protein levels of AdipoR1 and AdipoR2 decreased significantly after DOX injection. However, although the reduction of AdipoR2 was similar among the three groups, the reduction of AdipoR1 was less in the APN-SE group. The ratio of phosphorylated-AMPK-α (p-AMPK-α) to AMPK-α protein significantly decreased after DOX injection in the WT and APN-AS groups but increased in the APN-SE group. The ratio of cleaved caspase-3 to caspase-3 protein increased after DOX injection in all groups, but that in the APN-AS group was higher than that in the WT group, and that in the APN-SE group was lower than that in the WT group. The expression of Bax protein significantly increased after DOX injection in the WT and APN-AS groups but was suppressed in the APN-SE group. In contrast, the expression of Bcl-2 protein significantly decreased after DOX injection in the WT and APN-AS groups but was preserved in the APN-SE group (*Figure 3B*).

3.4 Apoptotic changes of cardiomyocytes *in vitro*

The percentage of viable cells was significantly higher in the APN-high group than in the APN-medium and saline groups. In contrast, the degree of caspase-3 activity was significantly lower in the APN-high group than in the APN-medium and saline groups. After the addition of AMPK inhibitor (AMPK-I), these changed in the APN-high group (*Figure 4A*). The numbers of apoptotic cells, which were detected as TUNEL-positive nuclei, significantly increased after the addition of DOX to the APN-medium and saline groups but did not increase in the APN-high group. After the addition of AMPK-I, the numbers of apoptotic cells also increased in the APN-high group (*Figure 4B*). In reverse transcription (RT)–PCR analyses, mRNA expression of Bax significantly increased after the addition of DOX to the APN-medium and saline groups but was suppressed in the APN-high group. In the APN-high + AMPK-I group, this expression was up-regulated as doses of AMPK-I increased. In contrast, mRNA expression of Bcl-2 significantly decreased after the addition of DOX to the APN-medium and saline groups but did not decrease in the APN-high group. In the APN-high + AMPK-I group, this expression was down-regulated as doses of AMPK-I increased (*Figure 5A*). In western blotting analyses, expression of Bax significantly increased after the addition of DOX to the APN-medium and saline groups but was suppressed in the APN-high group. In the APN-high + AMPK-I group, this expression was up-regulated as doses of AMPK-I increased. In contrast, expression of Bcl-2 significantly decreased after the addition of DOX to the APN-medium and saline groups but not in the APN-high group. In the APN-high + AMPK-I group, this expression was down-regulated as doses of AMPK-I increased (*Figure 5B*). These changes were attenuated in the saline + AICAR group vs. the saline group. Moreover, the levels of AdipoR1 mRNA expression and protein significantly decreased after the addition of DOX in the APN-medium and saline groups but not in the APN-high group. In contrast, AdipoR2 expression decreased similarly in the APN-medium, saline, and APN-high groups (Supplementary material online, *Figure S1*). Their expressions did not change with the use of either AMPK-I or AICAR.

3.5 Mitochondria-triggered apoptosis of cardiomyocytes *in vitro*

In western blotting analyses, the ratio of p-AMPK-α to AMPK-α significantly decreased after the addition of DOX to the APN-medium and saline groups vs. their controls, but these changes were not significant compared with those of the APN-high group control. This ratio in the APN-high group significantly decreased after the addition of DOX as doses of AMPK-I increased. In contrast, the ratio of cleaved caspase-3 to caspase-3 significantly increased after the addition of DOX to the APN-medium and saline groups vs. their controls, but these changes were not significant compared with the APN-high group control. This ratio in the APN-high group significantly increased after the addition of DOX as doses of AMPK-I increased (*Figure 6A*). Furthermore, mitochondrial cytochrome *c* significantly decreased and cytoplasmic cytochrome *c* significantly increased after the addition of DOX to the APN-medium and saline groups vs. their controls, but these changes were not significant compared with those of the APN-high group control. In the APN-high + AMPK-I group, mitochondrial cytochrome *c* significantly decreased and cytoplasmic cytochrome *c* significantly increased after the addition of DOX as doses of AMPK-I increased (*Figure 6B*). These changes were attenuated in the saline + AICAR group vs. the saline group.

4. Discussion

This study is the first to show that APN is cardioprotective in the context of DOX-induced chronic cardiomyopathy. We found that AMPK-dependent anti-apoptotic function is associated with cardioprotection. This conclusion was supported by the findings that the AMPK inhibitor dorsomorphin increased the pro-apoptotic factor Bax, suppressed the anti-apoptotic factor Bcl-2, and increased DOX-induced cardiomyocyte apoptosis through increased caspase-3 activity.

APN-AS mice showed deterioration of LV function following DOX-induced cardiomyopathy compared with WT mice. Conversely, APN-SE mice showed the maintenance of high plasma APN levels after DOX injection vs. attenuated detrimental LV dysfunction at 14 days in WT mice. Thus, we conclude that APN protects against the development of LV dysfunction, primarily by inhibiting the pathological apoptotic process that occurs in cardiomyocytes.

In our study, AMPK-α phosphorylated at the Thr^{172} residue, the activated form of AMPK,[27] was increased in APN-SE mice compared with WT mice. The increase in the ratio of cellular adenosine monophosphate to adenosine triphosphate is a major regulator of AMPK activity.[28] Recently, however, adipocyte-derived hormones also have been reported to activate AMPK.[29] Most of the beneficial effects of APN appear to be mediated by AMPK-associated signalling.[13,14] Our study demonstrated that the cardioprotective effects of APN after DOX-induced cardiomyopathy involve the AMPK signalling pathway.

Our *in vitro* experiment results showed that cytochrome c was transferred from the mitochondria into the cytoplasm and then activated cleaved caspase-3 in DOX-induced cardiomyopathy. Apoptosis is known to be a tightly regulated and evolutionarily conserved

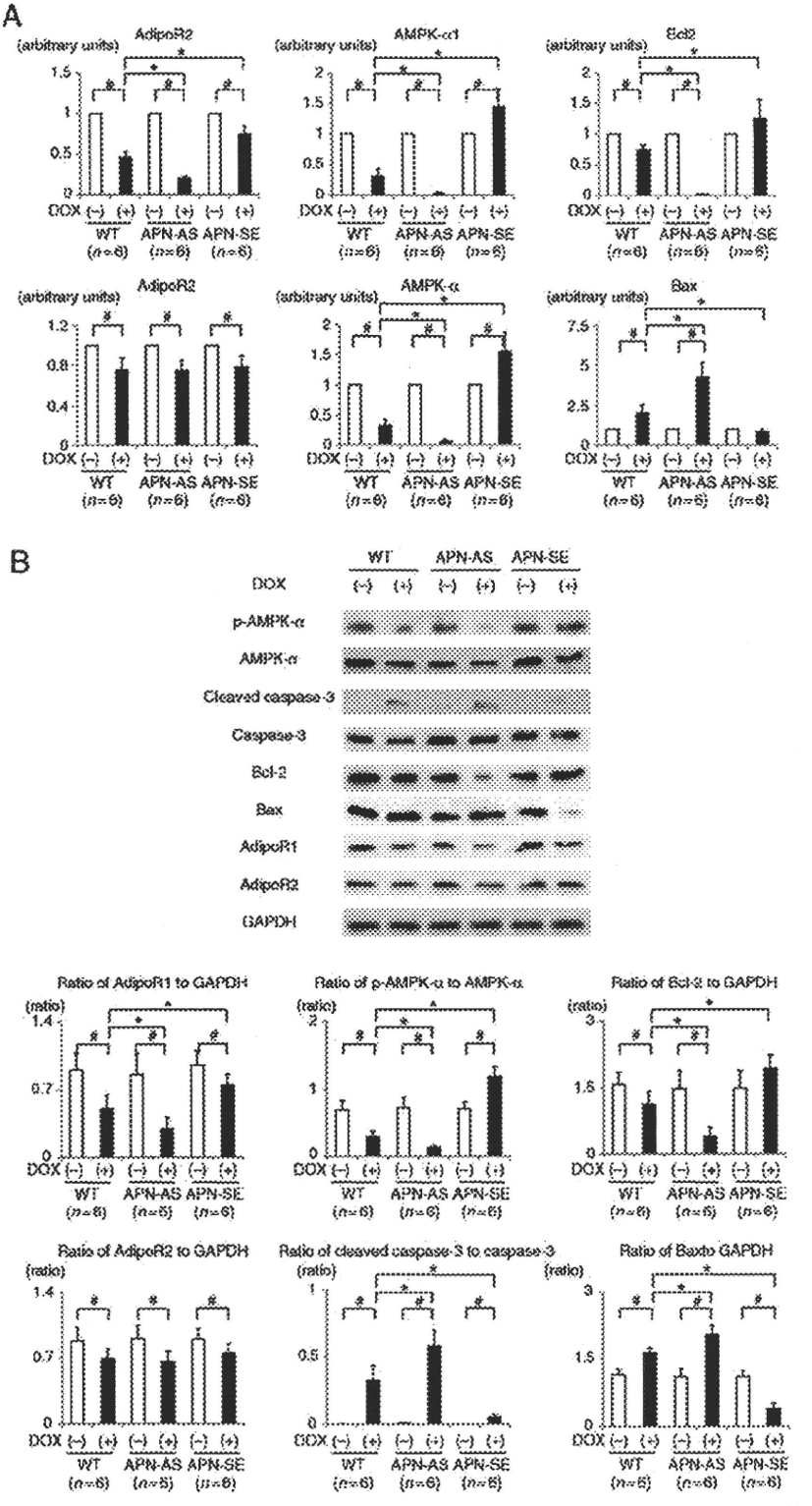

Figure 3 (*A*) mRNA expression levels of myocardium after 14 days in the WT ($n = 6$), APN-SE ($n = 6$), and APN-AS ($n = 6$) groups. (*B*) Western blotting analysis of myocardium after 14 days in the WT ($n = 6$), APN-SE ($n = 6$), and APN-AS ($n = 6$) groups. Open bars indicate the vehicle-injected mice of each group; closed bars indicate the DOX-injected mice of each group. $^{\#}P < 0.05$ compared with the vehicle-injected mice of each group. $^{*}P < 0.05$ compared with the WT group after DOX injection.

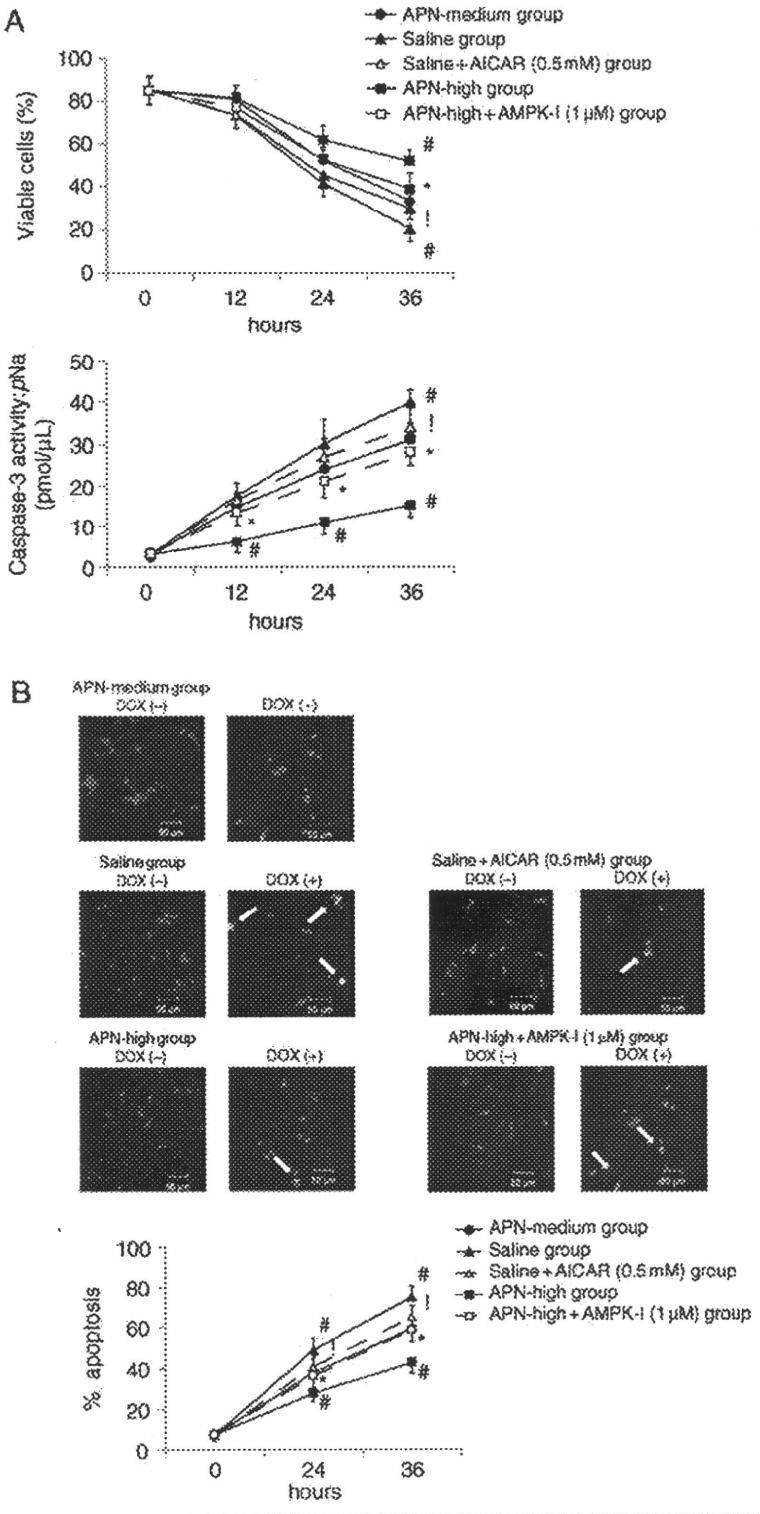

Figure 4 (*A*) Analysis of cellular viability and caspase-3 activity in the APN-medium ($n = 6$), saline ($n = 6$), saline + AICAR (0.5 mM) ($n = 6$), APN-high ($n = 6$), and APN-high + AMPK-I (1 μM) ($n = 6$) groups. (*B*) Analysis of apoptosis by the TUNEL methods of DOX-treated cells in the APN-medium ($n = 6$), saline ($n = 6$), APN-high ($n = 6$), and APN-high + AMPK-I (1 μM) ($n = 6$) groups. All pictures were taken 24 h after the last addition of saline or DOX. Arrows indicate TUNEL-positive nuclei. $^{\#}P < 0.05$ compared with the APN-medium group. $^{!}P < 0.05$ compared with the saline group. $^{*}P < 0.05$ compared with the APN-high group.

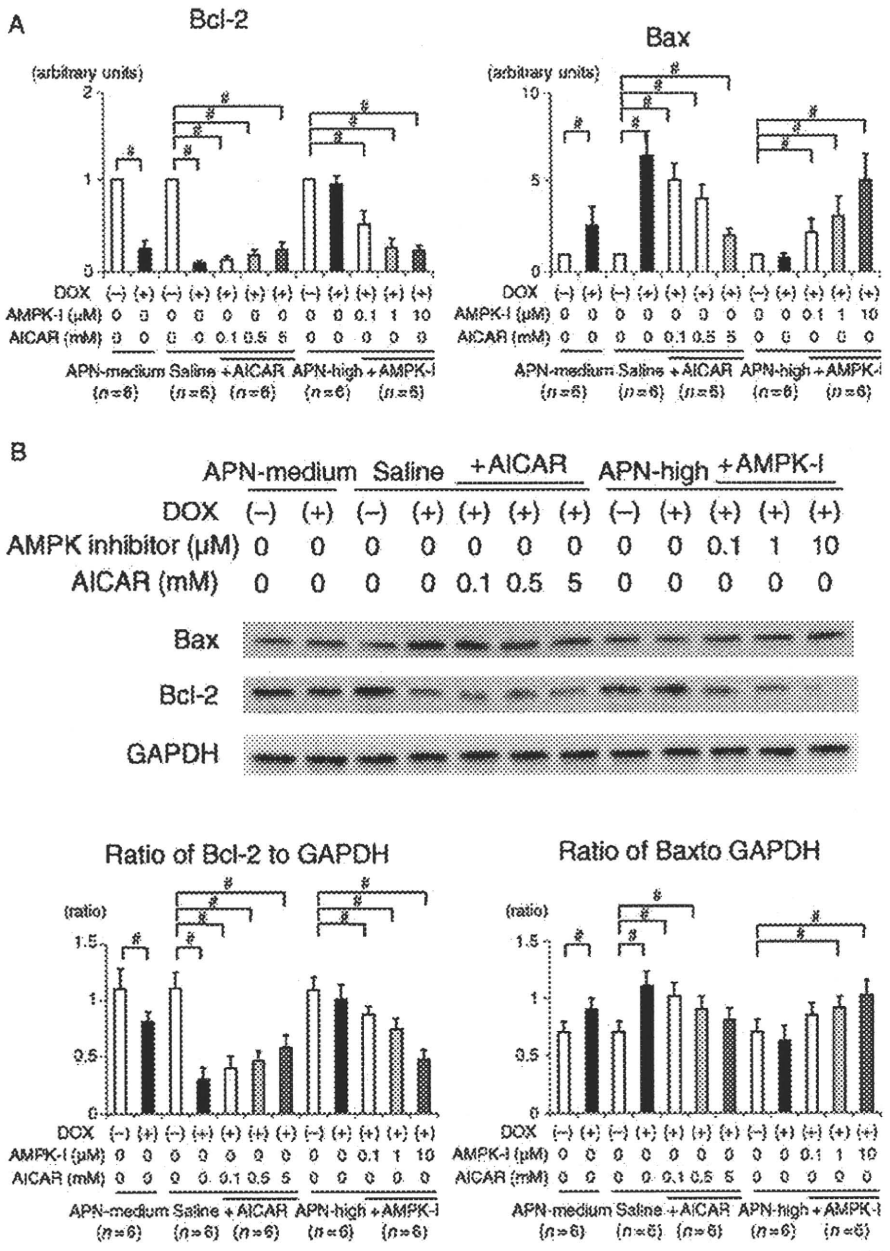

Figure 5 mRNA expression levels (*A*) and western blotting analysis (*B*) of Bcl-2 and Bax *in vitro* after 24 h in the APN-medium ($n = 6$), saline ($n = 6$), saline + AICAR (0.1 mM) ($n = 6$), saline + AICAR (0.5 mM) ($n = 6$), and saline + AICAR (5 mM) ($n = 6$), APN-high ($n = 6$), APN-high + AMPK-I (0.1 μM) ($n = 6$), APN-high + AMPK-I (1 μM) ($n = 6$), and APN-high + AMPK-I (10 μM) ($n = 6$) groups. Open bars indicate the vehicle-injected cells of each group; closed bars indicate the DOX-treated cells of each group. $^{\#}P < 0.05$ compared with the control of each group.

process. Mitochondria have been confirmed to play a critical role in apoptosis.[30] Physiological and pathogenic death signals by mitochondria-dependent death pathways may result in cytochrome *c* release. Cytochrome *c* released from the mitochondria to the cytoplasm activates caspase-9, which activates the caspase-3 effector and leads to apoptotic cell death.[31] Our *in vivo* and *in vitro* experiment results showed that Bcl-2 was up-regulated and Bax was down-regulated after DOX injection in proportion to the doses of APN and AMPK-α phosphorylation. Members of the Bcl-2 family are key regulators of apoptosis and are divided into the following groups: (i) anti-apoptotic members including Bcl-2 and (ii) pro-apoptotic members including Bax. Anti-apoptotic Bcl-2 can interfere with cytochrome *c* release and suppress apoptosis progression. In response to apoptotic stimuli, Bax overexpression with conformational changes counters the death repressor activity of Bcl-2, stimulates the release of cytochrome *c* and other apoptogenic proteins into the cytoplasm, and ultimately initiates apoptosis.[32]

We also observed the effect of APN in an acute DOX-induced cardiotoxicity model.[19] The survival rate in the APN-SE group was significantly higher than the WT and APN-AS groups (data not

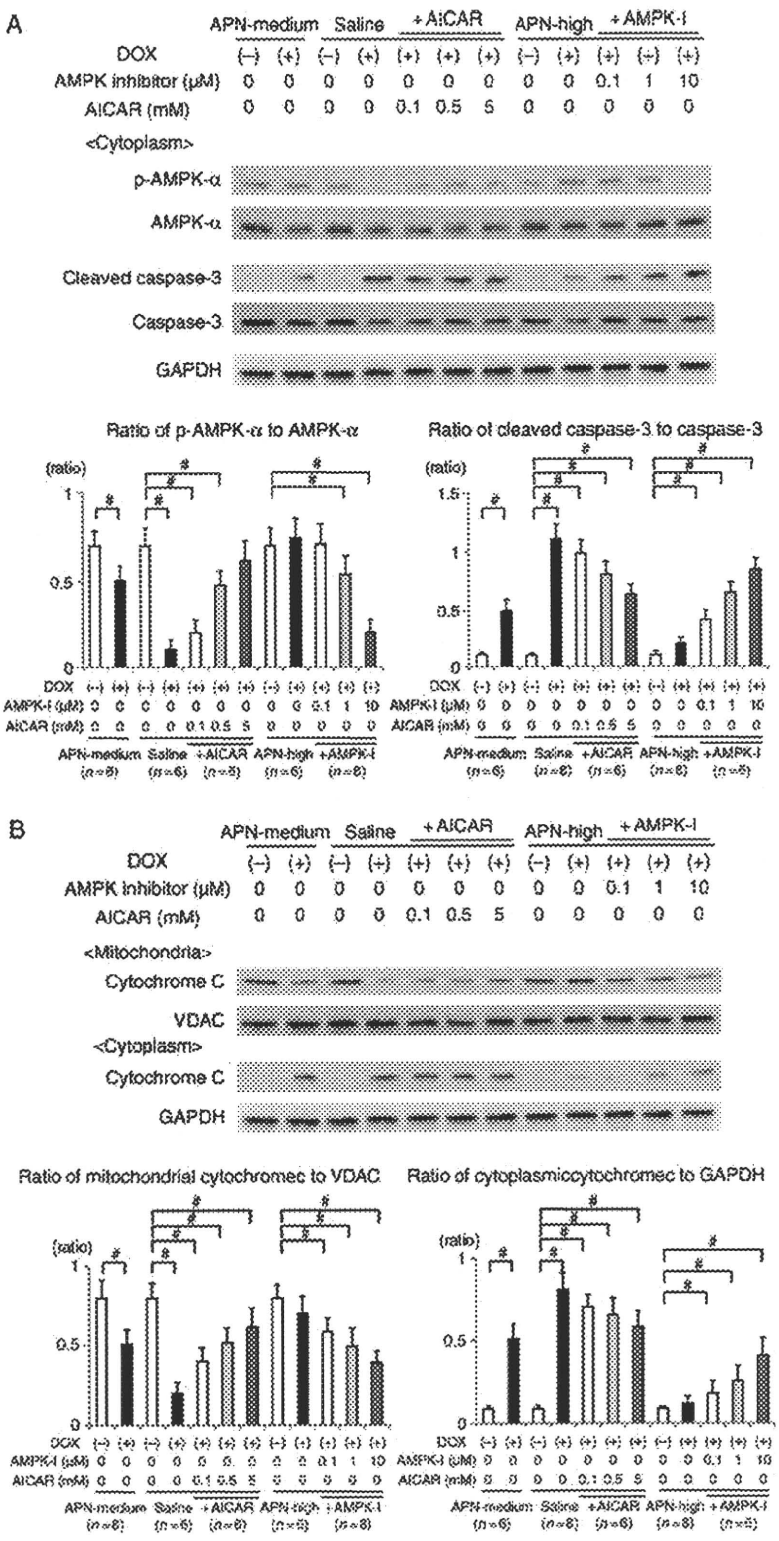

Figure 6 (*A* and *B*) Western blotting analysis of the cytoplasm and total mitochondrial extracts of cardiomyocytes *in vitro* after 24 h in the APN-medium ($n = 6$), saline ($n = 6$), saline + AICAR (0.1 mM) ($n = 6$), saline + AICAR (0.5 mM) ($n = 6$), and saline + AICAR (5 mM) ($n = 6$), APN-high ($n = 6$), APN-high + AMPK-I (0.1 μM) ($n = 6$), APN-high + AMPK-I (1 μM) ($n = 6$), and APN-high + AMPK-I (10 μM) ($n = 6$) groups. Open bars indicate the vehicle-injected cells of each group; closed bars indicate the DOX-treated cells of each group. $^{\#}P < 0.05$ compared with the control of each group.